COMPACTION OF Li-N-H BASED HYDROGEN STORAGE FOR KINETIC IMPROVEMENT AND SUPPRESSION OF NH$_3$ RELEASE

CHONGSUTTHAMANI SITTHIWET

A Thesis Submitted in Partial Fulfillment of the Requirements for the

Degree of Doctor of Philosophy in Chemistry

Suranaree University of Technology

Academic Year 2022

การกดอัด Li-N-H ในการเก็บไฮโดรเจน เพื่อการปรับปรุง คุณสมบัติทางจลนศาสตร์ และยับยั้งการปลดปล่อย NH_3

นางสาวจงสุทธามณี สิทธิเวช

COMPACTION OF Li-N-H BASED HYDROGEN STORAGE FOR KINETIC IMPROVEMENT AND SUPPRESSION OF NH$_3$ RELEASE

Suranaree University of Technology has approved this thesis submitted in partial fulfillment of the requirements for the Degree of Doctor of Philosophy.

Thesis Examining Committee

_____

(Assoc. Prof. Dr. Anyanee Kamkaew)

Chairperson

_____

(Assoc. Prof. Dr. Rapee Utke)

Member (Thesis Advisor)

_____

(Dr. Priew Eiamlamai)

Member (Thesis Co-Advisor)

_____

(Dr. Narong Chanlek)

Member

_____

(Assoc. Prof. Dr. Theeranun Siritanon)

Member

_____

(Assoc. Prof. Dr. Yupaporn Ruksakulpiwat)

Acting Vice Rector for Academic Affairs

and Quality Assurance

_____

(Prof. Dr. Santi Maensiri)

Dean of Institute of Science

จงสุทธามณี สิทธิเวช : การกดอัด Li-N-H ในการเก็บไฮโดรเจน เพื่อการปรับปรุงคุณสมบัติทางจลนศาสตร์ และยับยั้งการปลดปล่อย NH₃ (COMPACTION OF Li-N-H BASED HYDROGEN STORAGE FOR KINETIC IMPROVEMENT AND SUPPRESSION OF NH₃ RELEASE) อาจารย์ที่ปรึกษา : รองศาสตราจารย์ ดร.ระพี อูทเคอ, 56 หน้า

คำสำคัญ: การดูดซับไฮโดรเจน/ ไฮไดรด์ของโลหะ/ จลนพลศาสตร์ / ท่อนาโนคาร์บอน/ การจัดเก็บไฮโดรเจน/ โลหะทรานซิชัน/ การผันกลับได้/ การปลดปล่อยไฮโดรเจน

ลิเธียมเอไมด์ ($LiNH_2$) เป็นหนึ่งในวัสดุที่มีแนวโน้มในการกักเก็บไฮโดรเจนได้ดี เนื่องจากมีปริมาณไฮโดรเจนตามทฤษฎีสูง (8.7 wt. %) อย่างไรก็ตาม ก๊าซแอมโมเนีย (NH_3) ที่ปล่อยออกมาระหว่างการสลายตัวของ $LiNH_2$ จะเป็นพิษต่อตัวเร่งปฏิกิริยาของเซลล์เชื้อเพลิง (PEMFCs) แม้ว่าจะใช้สารประกอบไฮไดรด์ (RHC) ระหว่าง $LiNH_2$ และ LiH ที่สามารถแก้ปัญหานี้ได้ แต่มีการสังเกตว่ามีการปล่อย NH_3 บางส่วนและจลนพลศาสตร์ที่ไม่ดีด้วยเมื่อจำนวนรอบที่เพิ่มขึ้น จึงมีการเสนอวิธีการบดผสมสารด้วยลูกบอลที่ใช้พลังงานการหมุนสูงรวมทั้งเติมตัวเร่งปฏิกิริยาและสารเติมแต่งจำพวกคาร์บอนเพื่อปรับปรุงคุณสมบัติทางจลนพลศาสตร์ของสารประกอบ $LiNH_2$-LiH ในงานปัจจุบัน มีการแสดงผลของตัวเร่งปฏิกิริยาที่เป็นโลหะทรานซิชันแฮไลด์ (TiF_4) และท่อนาโนคาร์บอนที่มีผนังหลายชั้น (MWCNTs) ต่อประสิทธิภาพการปลดปล่อยและกักเก็บไฮโดรเจนของ $LiNH_2$-LiH ที่ถูกกดอัดและบรรจุในถังเก็บไฮโดรเจนขนาดเล็ก ซึ่งแสดงผลการเร่งปฏิกิริยาของ TiF_4 ต่อการแตกตัว/การรวมตัวกันใหม่ของไฮโดรเจนรวมถึงการนำความร้อนที่ดีขึ้นและการซึมผ่านของไฮโดรเจนจากท่อ MWCNTs และเป็นประโยชน์ต่อการดูดซับไฮโดรเจนที่แสดงในผลการทดลองโดยปฏิกิริยาแบบขั้นตอนเดียวและอุณหภูมิที่ต่ำกว่าในช่วง 150-350 °C (100 °C จาก $LiNH_2$-LiH ที่ไม่มีตัวเร่งปฏิกิริยาและสารเติมแต่งที่ถูกกดอัดเช่นเดียวกัน) ร่วมกับช่วงอุณหภูมิที่ราบและอัตราการไหลของไฮโดรเจนคงที่ (50 sccm) สูงสุด 30 นาทีระหว่างกระบวนการปลดปล่อยไฮโดรเจนด้วยแทงค์กักเก็บสารขนาดเล็ก ความจุของไฮโดรเจนในระหว่างรอบการกักเก็บและปลดปล่อยไฮโดรเจน เพิ่มขึ้นจาก 1.90-2.40 เป็น 3.10-4.70 โดยน้ำหนัก % H_2 (ตั้งแต่ 29 ถึง 80% ของความจุทางทฤษฎี) ที่น่าสนใจคือ Li_5TiN_3 ที่ตรวจพบได้จากการหมุนเวียนรอบการกักเก็บและปลดปล่อยไฮโดรเจน จะดูดซับ NH_3 เพื่อสร้างสารประกอบ $Li_5TiN_3(NH_3)_x$ มีส่วนสนับสนุนคุณสมบัติการดูดซับไฮโดรเจนของระบบ $LiNH_2$-LiH อย่างไรก็ตาม การขยายตัว/การหดตัวของตัวอย่างเม็ดเมื่อรอบการกักเก็บและปลดปล่อยไฮโดรเจนเพิ่มขึ้น ส่งผลให้เกิดการเสียรูปและ/หรือรอยแตก อาจทำให้เกิดการปลดปล่อย NH_3 ระหว่างจำนวนรอบที่มากขึ้น เช่นนี้จึงมีการเสนอแนวคิดในการประกบเม็ด $LiNH_2$-LiH ด้วยชั้นของสาร LiH ปริมาณ 10–30 wt. %

พบว่าเม็ด $LiNH_2$-LiH ที่ประกบด้วย LiH ไม่แสดงสัญญาณของการปล่อย NH_3 ด้วยความจุ H_2 3.5–4.0 wt. % ในรอบที่ 1 เมื่อวนเป็นรอบ (รอบที่ 2-6) การสลายตัวของเม็ด $LiNH_2$-LiH ที่ประกบด้วย 10 wt. % LiH แสดงสัญญาณ NH_3 ในขณะที่มี 30 wt. % LiH ปล่อยเฉพาะ H_2 ที่มีความจุ 2.3–2.6 โดยน้ำหนัก % H_2 ไม่เพียงแต่การปลดปล่อยไฮโดรเจนที่มีประสิทธิภาพและกระบวนการย้อนกลับของตัวอย่างที่มีน้ำหนัก 30 wt. % LiH-sandwiched $LiNH_2$-LiH ถูกอธิบายโดยผลการทดลองที่เพียงพอและความเสถียรเชิงกลของชั้น LiH ในเม็ดสารตัวอย่างเท่านั้น แต่ยังรวมถึงการก่อตัวของเฟสที่แอคทีฟใหม่ ($LiH_{1-x}F_x$ และ $Li_2NH_{1-y}F_y$) อีกด้วย

สาขาวิชาเคมี

ปีการศึกษา 2565

ลายมือชื่อนักศึกษา_____

ลายมือชื่ออาจารย์ที่ปรึกษา_____

ลายมือชื่ออาจารย์ที่ปรึกษาร่วม_____

CHONGSUTTHAMANI SITTHIWET : COMPACTION OF Li-N-H BASED HYDROGEN STORAGE FOR KINETIC IMPROVEMENT AND SUPPRESSION OF NH_3 RELEASE. THESIS ADVISOR : ASSOC. PROF. RAPEE UTKE. Ph.D. 56 pp.

Lithium amide ($LiNH_2$) is one of the most promising hydrogen storage materials due to its high theoretical hydrogen content (8.7 wt. %) and low cost. However, NH_3 gas released during $LiNH_2$ decomposition is poisonous for PEMFCs' catalysts. Although the reactive hydride composites (RHCs) between $LiNH_2$ and LiH can solve this problem, partial emission of NH_3 and poor kinetics with the enhanced cycling numbers are observed. High-energy ball milling as well as catalytic and additive doping have been proposed to improve the properties of $LiNH_2$-LiH composite. In the present work, the effects of transition metal-based catalyst (TiF_4) and multi-walled carbon nanotubes (MWCNTs) on de/rehydrogenation performance of compacted $LiNH_2$-LiH in small hydrogen storage tank are discussed. Catalytic effects of TiF_4 on hydrogen dissociation/recombination and the improved thermal conductivity and hydrogen permeability from MWCNTs benefit hydrogen sorption. The single-step reaction and lower temperature in range of 150-350 ℃ (100 ℃ lower than the compacted $LiNH_2$-LiH without additives) together with long plateau temperature and constant hydrogen flow rate (50 sccm) up to 30 min during dehydrogenation in the small tank are presented. The hydrogen capacities during de/rehydrogenation cycles increase from 1.90-2.40 to 3.10-4.70 wt. % H_2 (from 29 to up to 80% of theoretical capacity). Interestingly, Li_5TiN_3 detected upon cycling absorbs NH_3 to form $Li_5TiN_3(NH_3)_x$, favoring hydrogen sorption properties of $LiNH_2$-LiH system. However, the expansion/contraction of the pellet samples upon de/rehydrogenation cycles results in deformation and/or cracks. This possibly causes NH_3 release during cycling. The idea of sandwiching $LiNH_2$-LiH pellet with LiH layers (10–30 wt. %) is proposed. The LiH-sandwiched $LiNH_2$-LiH pellets show no sign of NH_3 release with the hydrogen capacitates of 3.5–4.0 wt. % H_2 in the 1st cycle. Upon cycling (the 2nd-6th cycles), the decomposition of LiH-sandwiched $LiNH_2$-LiH

pellets with 10 wt. % LiH shows NH_3 signal, while that with 30 wt. % LiH releases only hydrogen with the storage capacities of 2.3–2.6 wt. % H_2. Effective dehydrogenation and reversibility of the 30 wt. % LiH-sandwiched $LiNH_2$-LiH pellet are explained by not only sufficient content and mechanical stability of LiH layers but also the formation of the new active phases ($LiH_{1-x}F_x$ and $Li_2NH_{1-y}F_y$).

School of Chemistry

Academic Year 2022

Student's Signature _Chongsutthamani Sitthiwet_

Advisor's Signature _Rapee Uttu_

Co-advisor's Signature _____

ACKNOWLEDGEMENTS

This work would have never been accomplished without the contribution of many people. Firstly, I would like to thank my supervisor, Assoc. Prof. Dr. Rapee Utke for her expert guidance, support, discussions, encouragement, putting up with my moaning in many years, and always believing in me over the course of my thesis.

I also would like to thank my co-supervisor, Dr. Priew Eiamlamai from National Energy Technology Center, National Science, and Technology Development Agency for her great help and support and gratefully acknowledged for valuable help with the experimental work and kind suggestions during my visits to National Metal and Materials Technology Center.

I wish to gratefully acknowledge the financial support I have received from the Thailand Graduate Institute of Science and Technology (TGIST), Thailand (TG-33-19-60-015D) which enables me to continue my study after my bachelor's degree.

Also, I would like to thank all members of the Hydrogen Storage Material Lab and Solid-state Chemistry at SUT for their help, fulfillment, discussions, and friendship.

I would like to thank The Synchrotron Light Research Institute (Public Organization), Nakhon Ratchasima, Thailand, and the people from Mechanical workshop at Facility Building 1 (F1) SUT.

Finally, I would also like to thank my parents for their encouragement and moral support in every step of my academic career.

Chongsutthamani Sitthiwet

CONTENTS

CONTENTS (Continued)

LIST OF FIGURES

LIST OF FIGURES (Continued)

LIST OF FIGURES (Continued)

LIST OF TABLES

CHAPTER I

INTRODUCTION

1.1 Hydrogen energy

Alternative energies are of significant interest regarding the increase in global temperature, air pollution, and demand for fossil fuels with the depletion of crude oil resources. From Figure 1.1, the release of CO_2 per capita during 2001-2019 increases from 1.65 to 1.75 tCO_2/MWh in the afrika, whereas that in Europe decreases continuously to $\sim$ 1.00 tCO_2/MWh (Dematteis et al., 2021). These trends are the implementation of greater uses of renewable energies in Europe that are beneficial in the reduction of CO_2 emissions.
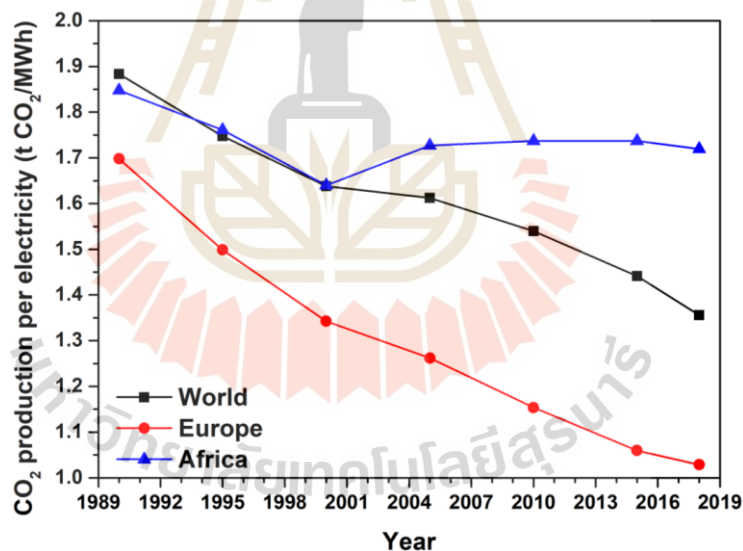
Figure 1.1 Global carbon dioxide (CO_2) production per electricity (Dematteis et al., 2021).

For Thailand, the government has drafted a plan to reduce greenhouse gas emissions, mostly from transportations and industries by aiming to increase the use of renewable.

energy up to 8-20% of the country's energy consumption within 2036(Thailand Power Development Plan, 2015). One of the most efficient renewable energies is hydrogen energy because of its high energy density (142 MJ kg^{-1}), great variety of sources (e.g., water, biomass, and organic matters), and low environmental impact (e.g., use in fuel cells) (Jain et al., 2010). Hydrogen is classified based on how the production process impacts the environment (Figure 1.2).
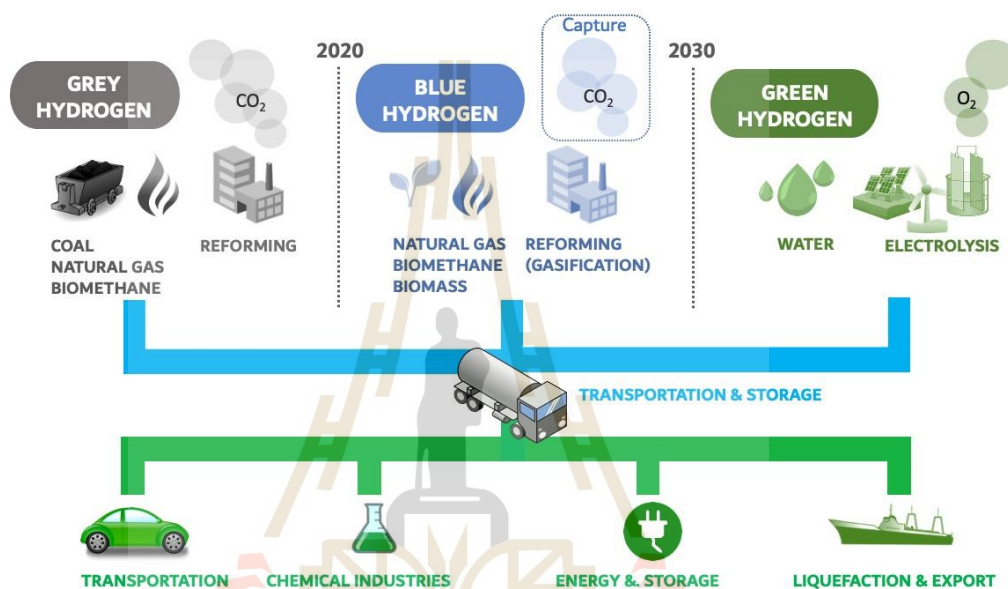
Figure 1.2 Visualization of the hydrogen production routes with a specific color. (http://www.chem4us.be/blue-green-gray-the-colors-of-hydrogen/).

Firstly, brown or gray hydrogen is produced by gasification or steam methane reforming (SMR) of hydrocarbon or fossil fuels. The products are a mixture of H_2 and CO_2. Therefore, this method does not reduce carbon even though hydrogen gas is clean energy. Next, blue hydrogen uses hydrocarbon or fossil fuels as raw materials, while the obtained CO_2 is captured and used to produce other forms of renewable fuels. (Carbon Capture & Storage Technology). The last one is green hydrogen, which produced no CO_2 emissions using clean electricity from renewable energy sources, such as solar or wind power, to electrolyze water splitting. Among all hydrogen types,

green hydrogen is the most environmentally friendly (Hydrogen, 2021). Hydrogen energy is classified into two categories according to applications, i.e., (1) portable energy storage systems often used in applications requiring fast charging, such as mobile phones and electric vehicles and (2) stationary energy storage systems. Hydrogen energy in all sections consists of productions, storages, and utilizations in the fuel cell system (Jena et al., 2011). From Figure 1.3, hydrogen is produced from water splitting using renewable sources (e.g., sun and wind) through an electrolyzer, stored in the storage tank, and supplied to fuel cells to produce electricity. (Sharaf and Orhan et al., 2014). Our work has been focused on hydrogen storage materials and systems.
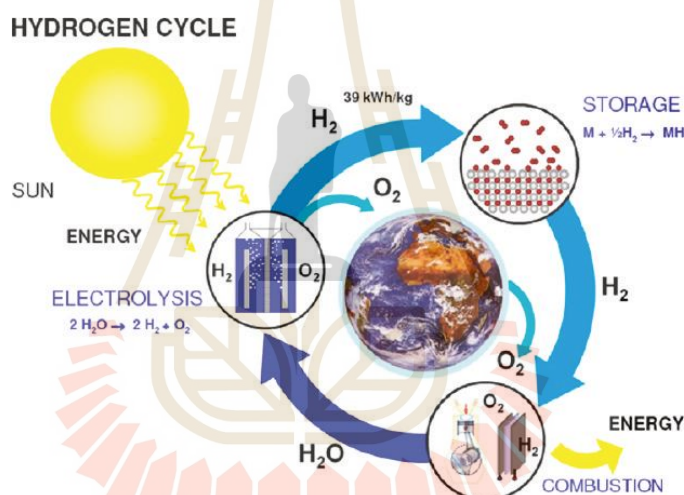
Figure 1.3 Hydrogen cycle (Jena, 2011).

2.2 Hydrogen storages methods and applications

Hydrogen can be stored by physical- and material-based methods (Figure 1.4) (Ren et al., 2017). For the physical-based method, the current technology practically used in the market is compressed hydrogen gas under 70 MPa with gravimetric and volumetric capacities of 5.7 wt. % H_2 and 40 gH_2/L, respectively. Although hydrogen capacities of the compressed gas is satisfied according to US-DOE targets (Table 2), its heavy and bulky tank as well as safety concerns due to high pressure still obstruct the practical uses. For cryogenic liquid, hydrogen is stored at low temperature (≤20K) to obtain higher volumetric hydrogen capacity (70 kgH_2m^{-3}). However, large thermal losses

and the cost of insulation for storage tanks and hydrogen stations hinder its applications. Thus, physically and chemically material-based storage methods have been proposed. Hydrogen can be stored physically in microporous materials with high surface area through Van der Waals interaction and chemically in metal and complex hydrides (Ren et al., 2017).
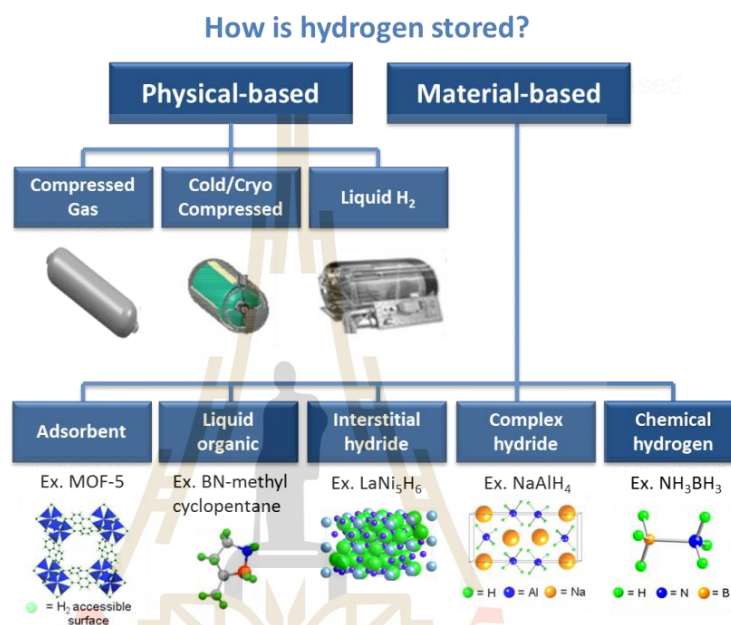
Figure 1.4 Hydrogen storage methods (Rambhujun et al., 2020).

Physisorption-based microporous materials include carbons, zeolites, and metal-organic frameworks (MOFs). They adsorb molecular hydrogen in their porous structures and hydrogen storage capacity depends on the specific surface area. In chemisorption, chemical reactions between metals or alloys with hydrogen provide high theoretical volumetric and gravimetric capacities of 40-120 kgH_2 m^{-3} and 5- 18 wt. % H_2, respectively. Nevertheless, high operating temperature and pressure conditions for de/rehydrogenation, for example, rehydrogenation of $LiBH_4$ at ~600 °C under 155 bar H_2 for >12 h (He et al., 2019), slow kinetics, and release of by-product gases poisoning fuel cell catalyst, and membranes (e.g., B_2H_6 from $LiBH_4$ and NH_3 from $LiNH_2$) (Yan et al., 2012) obstruct the application of hydrides as hydrogen storage materials.

Table 1.1 Targets of material-based automotive hydrogen storage systems set by the US-DOE. (https://www.energy.gov/eere/fuelcells/doe-technical-targets-onboard-hydro-gen-storage-light-duty-vehicles)

Storage System Targets	Gravimetric density (kg H_2/kg system)	Volumetric density (kg H_2/L system)	Temperature (°C)	Pressure (bar H_2)
2025	0.055	0.040	-40-85	5-12
Ultimate	0.065	0.050	-40-85	5-12
Current Status	Gravimetric density (kg H_2/kg system)	Volumetric density (kg H_2/L system)	Temperature (°C)	Pressure (bar H_2)
Metal Hydride (MH): NaAlH$_4$	12	12	125	0.2-10
Sorbent: MOF-5	38	21	-193	100
Chemical hydrogen (CH) Storage: Off-Board Regenerable (AB)	46	40	-	-

In this work, we aim not only to improve kinetics and hydrogen capacities of hydrides approaching the 2020 US-DOE targets (Table 1.2) (Huang et al., 2021) but also upscaling to hydrogen storage tank. Among several solid-state hydrides, lithium amide (LiNH$_2$) is one of the most promising materials for reversible hydrogen storages because it contains high theoretical hydrogen content of 8.7 wt. % (Figure 1.5) (Miceli, 2010). However, ammonia (NH$_3$) released upon decomposition of LiNH$_2$ (equation (1.1)), toxic to fuel cell catalysts must be suppressed (Yao et al., 2007).

$$2LiNH_2 \; \rightarrow \; Li_2NH + NH_3 \tag{1.1}$$
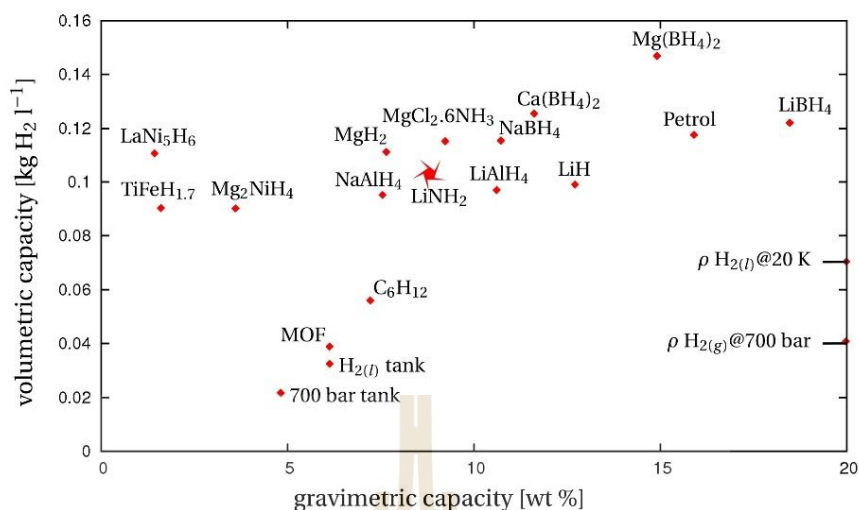
Figure 1.5 Theoretical hydrogen storage capacities of hydrogen storage materials (Miceli, G. (2010)).

To use $LiNH_2$ as hydrogen storage material, reactive hydride composites (RHCs) between $LiNH_2$ and other hydrides, such as $LiNH_2$-MgH_2 (Xilin et al., 2014), $LiNH_2$-$LiAlH_4$ (Dolotko et al., 2011), $LiNH_2$-$LiBH_4$ (Liu et al., 2009), $LiNH_2$-MgH_2-$LiBH_4$ (Wang et al., 2015), and $LiNH_2$-$Ca(BH)_4$ (Yua et al., 2011) have been proposed. Among all $LiNH_2$-based composites, $LiNH_2$-LiH is one of the best-performing materials for storing hydrogen due to its relatively low operating temperature, good reversibility, and low cost (Fernandez et al., 2013). Nevertheless, partial emission of NH_3 as well as poor kinetics, especially with the enhanced cycling numbers are observed. Thus, this work focuses on kinetic improvement and suppression of NH_3 release of $LiNH_2$-LiH composite by compaction into the pellets and sandwiching with LiH layer. Moreover, hydrogen storage performance in the small hydrogen storage tank is studied.

1.3 References

Dematteis, E.M., Barale, J., Corno, M., Sciullo, A., Baricco, M., and Rizzi, P. (2021). Solid-State Hydrogen Storage Systems and the Relevance of a Gender Perspective. *Energies, 14,* 6158. doi: 10.20944/preprints202106.0617.v1

Dolotko, O., Kobayashi, T., Wiench, J.W., Pruski, M., and Pecharsky, V. (2011). Investigation of the thermochemical transformationsin the $LiAlH_4$-$LiNH_2$ system. *Int. J. Hydrogen Energy, 36,* 10626-10634. doi: 10.1016/j.ijhydene.2011.05.163

Fernandez Albanesi, L., Arneodo Larochette, P., and Gennari, F.C. (2013). Destabilization of the $LiNH_2$-LiH hydrogen storage system by aluminum incorporation. *Int. J. Hydrogen Energy, 38,* 12325-12334. doi: 10.1016/j.ijhydene.2013.07.030

Huang, Y., Cheng, Y., and Zhang, J. (2021). A Review of High Density Solid Hydrogen Storage Materials by Pyrolysis for Promising Mobile Applications. *Ind. Eng. Chem. Res., 60,* 2737–2771. doi: 10.1021/acs.iecr.0c04387

Hydrogen. (2021). Types of hydrogen. *[On-line]. Avialable: https://aureliaturbines.com /articles.*

Jain, I.P., Lal, C., and Jain, A. (2010). Hydrogen storage in Mg: A most promising material. *Int. J. Hydrogen Energy, 35,* 5133-5144. doi: 10.1016/j.ijhydene.2009.08.088

Jena, P. (2011). Materials for Hydrogen Storage: Past, Present, and Future. *J. Phys. Chem. Lett, 2,* 206–211. doi: 10.1021/jz1015372

Liu, Y., Luo, K., Zhou, Y., Gao, M., and Pan, H. (2009). Diffusion controlled hydrogen desorption reaction for the $LiBH_4$/$2LiNH_2$ system. *J. Alloys Compd, 481,* 473–479. doi: 10.1016/j.jallcom.2009.02.142

Miceli, G. (2010). First principles study of the $LiNH_2$/Li_2NH hydrogen storage system. *Ph.D., Thesis.*

Ren, J., Musyoka, N.M., Langmi, H.W., Mathe, M., and Liao, S. (2017). Current research trends and perspectives on materials-based hydrogen storage solutions: A critical review. *International Journal of Hydrogen Energy, 42*(1), 289-311. doi: 10.1016/j.ijhydene.2016.11.195

Rambhujun, N., Salman, M.S., Wang, T., Pratthana, C., Sapkota, P., Costalin, M., Lai, Q., and Aguey-Zinsou, K.F. (2020). Renewable hydrogen for the chemical industry. *MRS Energy and Sustainability,7,* e33. doi: 10.1557/mre.2020.33

Sharaf, O.Z., and Orhan, M.F. (2014). An overview of fuel cell technology: Fundamentals and applications. *Renewable and Sustainable Energy Reviews, 32,* 810-853. doi:10.1016/j.rser.2014.01.012

Thailand Power Development Plan 2015-2036 (PDP2015) (2020) *[On-line]. Available: https://www.egat.co.th/en/images/about-egat/PDP2015_Eng.pdf.*

Wang, Z., Lijun, J., Yuanfang, W., Jianhua, Y., Baolong, Y., Zhinian, L., Xiaopeng, L., and Shumao, W. (2015). Improved dehydrogenation cycle performance of the $1.1MgH_2$-$2LiNH_2$-$0.1LiBH_4$ system by addition of $LaNi_{4.5}Mn_{0.5}$ alloy. *J. Rare Earths, 33,* 783. doi: 10.1016/S1002-0721(14)60485-3

Xilin, Z., Shumin, H., Xin, Z., Yuan, L., and Baozhong, L. (2014). Effect of lanthanum hydride on microstructures and hydrogen storage performances of $2LiNH_2$-MgH_2 system. *J. Rare Earths, 32,* 429-433. doi: 10.1016/S1002-0721(14)60089-2

Yan, Y., Remhof, A., Hwang, S.J., Li, H.W., Mauron, P., Orimo, S., Züttel, A. (2012). Pressure and temperature dependence of the decomposition pathway of LiBH4. *Phys Chem Chem Phys, 14*(18), 6514-6519. doi:10.1039/c2cp40131b

Yao, J.H., Shang, C., Aguey-Zinsou, K.F., and Guo, Z.X. (2007). Desorption characteristics of mechanically and chemically modified $LiNH_2$ and ($LiNH_2$ + LiH). *J. Alloys Compd, 432,* 277–282. doi: 10.1016/j.jallcom.2006.05.113

Yua, X.B., Yang, Z.X., Guo, Y.H., and Li, S.G. (2011). Thermal decomposition performance of $Ca(BH_4)_2$/$LiNH_2$ mixtures. *J. Alloys Compd, 509S,* S724– S727. doi: 10.1016/j.jallcom.2010.11.076

CHAPTER II
LITERATURE REVIEW

2.1 Hydrogen storage in metal hydrides

Hydrogen chemisorption in the forms of metal and complex hydrides consists of dissociation of hydrogen molecule, diffusion of hydrogen atoms into interstitial sites of metal and formation of M-H bond (Figure 2.1(A)). Nucleation and growth of hydride will occur under moderate temperatures and pressures following the pressure-composition (PCT) isotherms (Figure 2.1(B)(i)) (Klebanoff, 2016). The PCT curve is the correlation between the equilibrium pressure and the hydrogen storage content at temperature settings. The α-phase region corresponds to the formation of metal hydride at low pressures. The plateau region is in accordance with the equilibrium of α and β phases. Nucleation and growth of the metal hydride refer to β-phase region. The plateau region in the PCT plot indicates the reversible hydrogen content. Considering van't Hoff equation (2.1), enthalpy (ΔH) and entropy (ΔS) of hydride formation can be obtained from slope and y-intercept of the van't Hoff plot (Figure 2.1(B)(ii).

$$\ln(P_{eq}/P_0) = \frac{\Delta H}{RT} - \frac{\Delta S}{RT} \tag{2.1}$$

Where P_{eq} is the plateau pressure, T is the temperature, P_0 is the reference pressure (1 bar), R is the gas constant (R = 8.314 J.mol^{-1}. K^{-1}), ΔH and ΔS are the enthalpy and entropy changes, respectively.

The enthalpy of metal hydrides relates to the heat during hydrogen absorption and desorption. To obtain equilibrium pressure (P_{eq}) of 1 bar at 40-150 °C, an operating

temperature of fuel cell, ΔH of 30– 55 kJ/mol with constant ΔS (130 J/mol K) is required (Züttle, 2008).
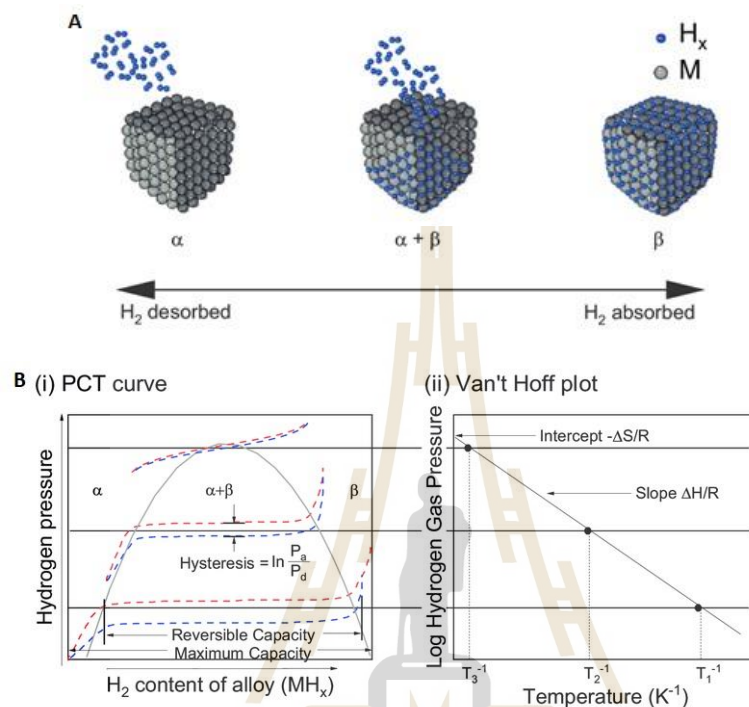
Figure 2.1 Hydride formation (α and β phase) (A), PCT curves (i) and van't Hoff plot (ii) (B) (Modi et al., 2021).

Thus, metal hydrides with high hydrogen capacity and suitable thermodynamic properties are challenging for hydrogen storage materials. Another barrier for the practical application of metal hydrides is kinetic, considering a rate-limiting step for a particular reaction. From Figure 2.2(A), during absorption hydrogen gas is physisorption onto the surface of metal hydride (step 1). Then, hydrogen molecules dissociate into atoms, further occupying and penetrating into the interstitial sites of the host metal (steps 2 and 3). When the amount of hydrogen increases, diffusion through the hydride layer occurs (step 4) to complete hydride formation. For desorption, metal hydride decomposes into metal and hydrogen (step 1). Hydrogen atom diffuses through metal (step 2) and to the surface (step 3). Finally,

the recombination of hydrogen atoms into molecules (step 4), releasing to the environment (step 5).
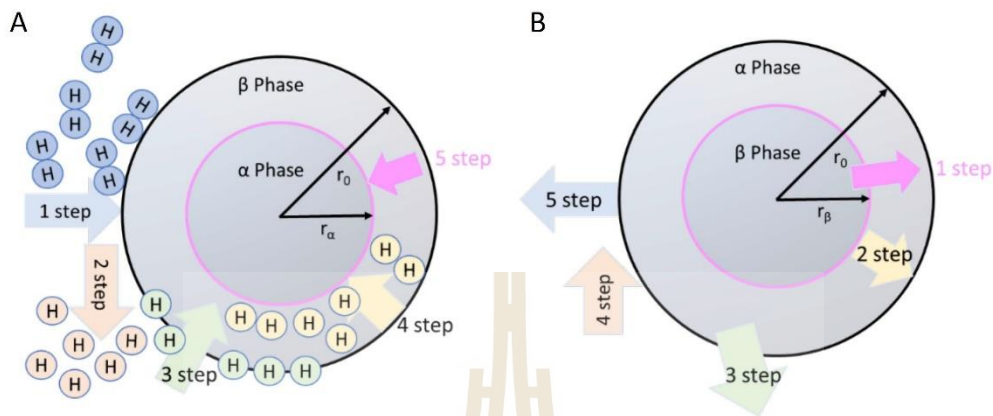
Figure 2.2 Steps for the absorption (A) and desorption (B) of the metal hydrides. (Jain et al., 2018).

The chemical reaction's activation energy (E_a) presents a barrier in the reaction pathway, in which many hydrides show significantly high Ea. To practically use metal hydride, rapid hydrogen de/rehydrogenation at moderate temperature is needed. Catalytic doping is of interest due to lowering Ea without any changes in chemical structures of reactants and products as well as thermodynamic properties (Züttle, 2008). Ea can be investigated by differential scanning calorimetry (DSC) technique and Kissinger equation (2.2).

$$\ln (\beta/T^2_p) = \frac{-Ea}{RTp} + \ln(k_0) \tag{2.2}$$

where β is the heating rate (°C/min), Tp is the peak desorption temperature, R is the gas constant (8.314 J mol^{-1} K^{-1}), Ea is the activation energy, and k_0 is a constant.

2.2 LiNH$_2$/Li$_2$NH and their tuning strategies

Although other metal hydrides and/or complex hydrides following Figure 1.5 have accomplished high gravimetric and volumetric hydrogen capacities, their dehydrogenation temperatures are still high due to the large enthalpy. LiNH$_2$/Li$_2$NH system is one of the most competitive materials for hydrogen storage because of their suitable gravimetric and volumetric capacities according to the U.S. (DOE) (5.5 wt. % and 40 gH$_2$/L, respectively) (Partnership., 2017). LiNH$_2$ consists of Li$^+$ cation and NH$_2^-$ anionic group with tetragonal by space group of *I-4*, which preferred an anti-fluorite with the arrangement of Li in a tetrahedral hole and N in a cubic close-packed. However, LiNH$_2$ decomposes into Li$_2$NH and NH$_3$ at 373-375 °C under vacuum (equation (2.3)) instead of hydrogen. Thus, LiNH$_2$-LiH composite has been proposed, which the obtained NH$_3$ further reacts with LiH to form Li$_2$NH and H$_2$ (equation (2.4)). However, the deterioration of LiH due to hydrolysis/oxidation led to NH$_3$ emission, resulting in poisoning proton exchange membranes (PEMFCs) and poor hydrogen capacity (Shaw et al., 2008). Moreover, poor kinetics due to slow NH$_3$ diffusion through the Li$_2$NH coated on the LiNH$_2$ core and deficient interfaces between LiH and NH$_3$ are serious issues (Chen et al., 2002). Regarding the previous work reported by Chen et al. (2003) and Chen et al. (2002), overall reaction for LiNH$_2$-LiH decomposition (equation (2.5)) provides the storage capacity of 6.5 wt. % H$_2$.

$$2LiNH_2 \quad \longrightarrow \quad Li_2NH + NH_3 \qquad (2.3)$$

$$2LiH + NH_3 \quad \longrightarrow \quad Li_2NH + 2H_2 \qquad (2.4)$$

$$LiNH_2 + LiH \quad \longrightarrow \quad Li_2NH + H_2 \qquad (2.5)$$

For Li$_2$NH, it has two crystal structures of *Fm-3m* and *Imma* space group as low-temperature (LT) and high-temperature (HT) phases, respectively (Juza, 1951). Phase transition of Li$_2$NH from the LT to the HT can be detected at 400-500 K. During the decomposition of LiNH$_2$, the rate-limiting step is NH$_3$ formation at the interface of LiNH$_2$/Li$_2$NH (Figure 2.3).
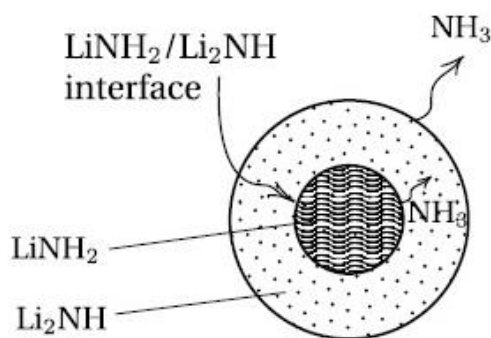
Figure 2.3 The decomposition path of the $LiNH_2/Li_2NH$ (Miceli et al., 2010).

Several approaches to improve de/rehydrogenation kinetics and suppress NH_3 emission of $LiNH_2$-LiH composites, including nanoparticle preparation and catalytic doping have been reported. Varin et al. (2010) studied the effects of milling time and $LiNH_2$: LiH molar ratio. When the milling time increased up to 25 h, the grain size of $LiNH_2$-LiH composite decreased, enhancing specific surface area. (Figure 2.4(A)).
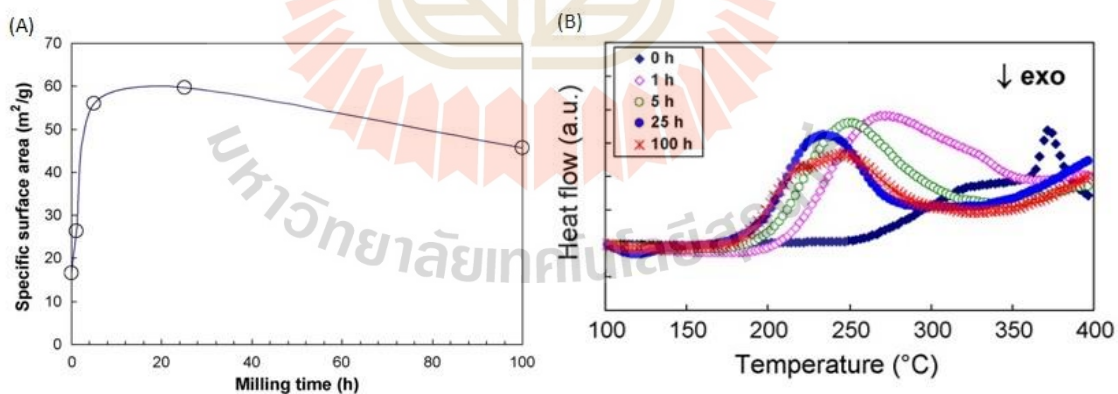
Figure 2.4 The specific surface area to ball milling time of the $LiNH_2$-LiH composite (A) and DSC profiles for varied milling time (B).

Dehydrogenation temperature decreased with the increase of milling time up to 25 h (Figure 2.4(B)). From Table 2.1, not only milling time but also the enhancement of LiH content benefits dehydrogenation kinetics.

Table 2.1 Summary of the DSC profiles for $LiNH_2$-LiH by varied milling time and LiH molar ratio.

Milling time (h)	Molar ratio ($LiNH_2$-LiH)	DSC peak (°C)	
		T (onset)	T (main)
0	1:1	268	324.7
1	1:1	212	272.5
5	1:1	196.2	250.2
25	1:1	186	235.2
25	1:1.2	183.4	239.2
25	1:1.4	180.3	234.1
100	1:1	187.2	245

When the milling time increased, the onset temperature decreases from 268 °C to 180 °C because most $LiNH_2$ could effectively react with LiH. The latter was explained by good contact between $LiNH_2$ and LiH particles. In the case of $LiNH_2$: LiH mole ratios increasing from 1:1 to 1:1.4, onset desorption temperature decreased because of excess LiH overcoming hydrolysis/oxidation into LiOH or Li_2O.

Furthermore, various additives and/or catalysts, such as metal hydrides (LiH, NaH, KH, MgH_2, CaH_2, and TiH_2 (Amica et al., 2015), graphite (Varin et al., 2011), nitrides, and Ti-Li-N compounds (TiN, BN and Li_5TiN_3 (Aguey-Zinsou et al., 2007), (Nayebossadri et al., 2011), (Du et al., 2015), halides ($AlCl_3$ (Ferna ́ndez Albanesi et al., 2013), $MgCl_2$ (Davies et al., 2015), CeF_4

(Lin et al., 2018), KF (Dong et al., 2016), RbF (Dong et al., 2017), amide KNH_2 (Ping et al., 2019), and oxides (LiOH, NaOH, KOH (Dong et al., 2015), and $LiTi_2O_4$ (Zhang et al., 2015) have been studied to improve hydrogen sorption properties of $LiNH_2$-LiH composite. Amica et al. (2015) studied chemical interactions during hydrogen cycling of $LiNH_2$-1.6LiH doped with MH_2 (M = Mg, Ca, Ti). The results showed that $LiNH_2$ doped with MgH_2 and CaH_2 produced the solid solutions of $Li_2Mg(NH)_2$ and $CaNH-Ca(NH_2)_2$, revealing superior de/rehydrogenation kinetics (Figure 2.5). However, TiH_2 showed poorer kinetics with respect to MgH_2 - and CaH_2 – doped samples. This can be explained by the fact that TiH_2 presented direct contact with $LiNH_2$ and LiH, whereas MgH_2 and CaH_2 interacted with $LiNH_2$. Furthermore, Dong et al. (2016) reported the positive effects of potassium fluoride (KF) on the $LiNH_2$-LiH composite, in which the cycling stability of $LiNH_2$-LiH was enhanced after doping with KF (Figure 2.6).
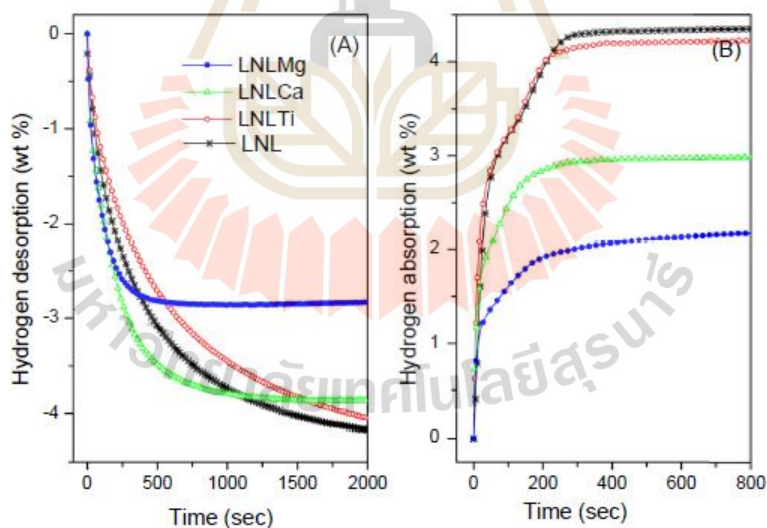
Figure 2.5 Dehydrogenation under 0.02 MPa (A) and rehydrogenation under 0.7 MPa hydrogen pressure (B) at 300 °C of the $LiNH_2$-1.6LiH and doping with MH_2 (M = Mg, Ca, and Ti).

Potassium hydride (KH) formed during ball milling of $LiNH_2$-LiH doped with KF acted as active species to improve hydrogen storage properties since it could react with NH_3 to produce KNH_2 and release hydrogen (equation 2.6).

$$KH + NH_3 \quad \rightarrow \quad KNH_2 + H_2 \quad\quad\quad (2.6)$$

Lin et al. (2018) reported kinetic improvement of the $LiNH_2$-LiH system with 10 wt. % cerium-based materials (Ce, CeO_2, CeF_3, and CeF_4) (Figure 2.7).
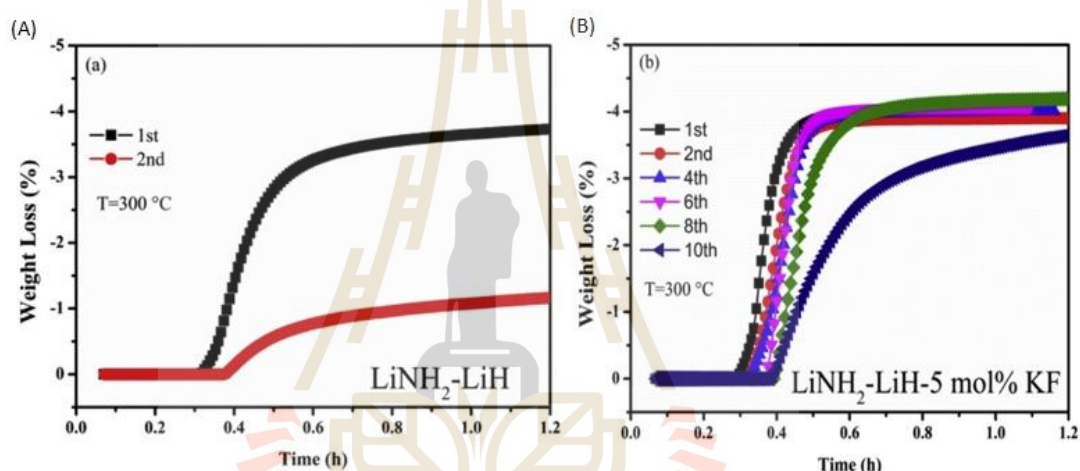
Figure 2.6 Cycling stability of $LiNH_2$-LiH (A) and $LiNH_2$-LiH-5mol%KF (B).

The best kinetic improvement and suppression of NH_3 emission was obtained from the sample doped with CeF_4. It was found that CeF_x species formed during the ball milling process was a good catalyst for $LiNH_2$ decomposition without NH_3 emission. Moreover, some active intermediate of Li_5TiN_3 found after ball milling of $LiNH_2$-LiH-Ti-based compounds (e.g., Ti, $TiCl_3$, and TiO_2) acted as NH_3 carriers from $LiNH_2$ to LiH on a nanometer scale in the forms of $Li_5TiN_3(NH_3)_x$ (Teng et al., 2011).

For carbon materials, Varin et al. (2011) proposed that doping graphite (5 wt. %) into $LiNH_2$-1.2LiH showed an increase in the de/absorbed capacities at 325 °C from 4.7 to

5.2 wt. % H_2 as well as superior reversibility with 5 wt. % H_2. It was suggested that graphite could prevent or reduce the oxidation/hydrolysis of LiH due to the water repelling from its surface. Moreover, hydrogen diffusion and heat transfer of hydride materials could be enhanced by several carbon materials, such as multi-walled carbon nanotubes (MWCNTs), activated carbon, graphene, and carbon nanofibers (CNFs).
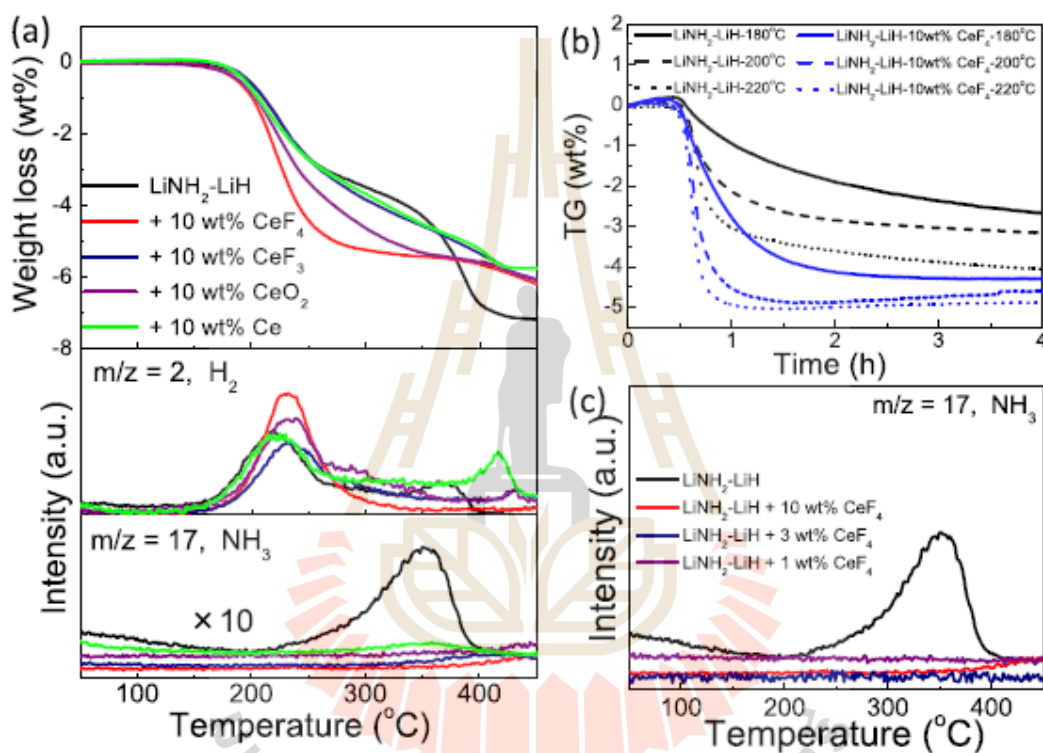
Figure 2.7 Dehydrogenation profiles of the $LiNH_2$-LiH composites and Ce- doped $LiNH_2$-LiH (a), Isothermal dehydrogenation of the $LiNH_2$-LiH composites and CeF_4-doped $LiNH_2$-LiH at different temperatures (b), and NH_3 signal in MS curves of CeF_4-doped $LiNH_2$-LiH (c).

2.3 Small hydrogen storage tanks for hydrogen storage materials

In practical applications, the hydride materials have to be packed into a closed tank. Experimental and numerical works have investigated the hydrogen sorption properties of the storage tanks. Chaise et al. (2010) and Chung et al. (2013) studied both experimental and numerical data on the de/rehydrogenation properties of the magnesium hydride-based hydrogen storage tank. They reported the enhancement of the hydrogen sorption rate by inserting heat pipes into a novel metal hydride tank. Also, heat transfer properties affecting hydrogen sorption properties were improved by inserting a heat exchanger (Wu et al., 2014). Besides tube heat exchanger, the thermal conductivity of hydride tanks was enhanced by integrating copper wire nets, aluminum foams, and hydride–graphite composites (Shim et al., 2014), (Mazzucco et al., 2014). Furthermore, the volumetric hydrogen storage capacities for hydrogen storage tanks can be enhanced by compacting metal hydride to the pellet (Lozano et al., 2011). Recently, Yan et al. (2015) designed a cylindrical lab-scale tank based on compaction of $Mg(NH_2)_2$–$2LiH$–$0.07KOH$ mixed with expanded natural graphite (ENG). The laboratory-scale hydrogen storage tank was designed with 205 mm and 32 mm of length and diameter, respectively. There was a porous filter tube placed in the tank center for the hydrogen diffusion pathway. In addition, three thermocouples were located in the hydride beds for measuring the temperature during de/rehydrogenation (Figure 2.8(A)). Dehydrogenation kinetics of the compacted $Mg(NH_2)_2$–$2LiH$–$0.07KOH$ mixed with up to 17 wt.% ENG were operated at 220 °C with a hydrogen flow rate of 0.6 L/min. Three regions (I, II, and III) during hydrogenation were characterized (Figure 2.8(B)). In region I, hydrogen pressure rapidly decreases and the temperature of the hydride bed is reduced when desorption occurs. For region II, the temperature decreases continuously together with hydrogen pressure drops due to the decomposition of hydrogen storage materials. The mass flow controller demonstrates hydrogen gas flows through with a constant flow rate until the pressure drops due to complete dehydrogenation.

Finally, region III is the hydrogen desorption almost finishes shown as the reduction of hydrogen flow rate less than 0.1 L/min, and the temperature in the tank increases to the set-point temperature.
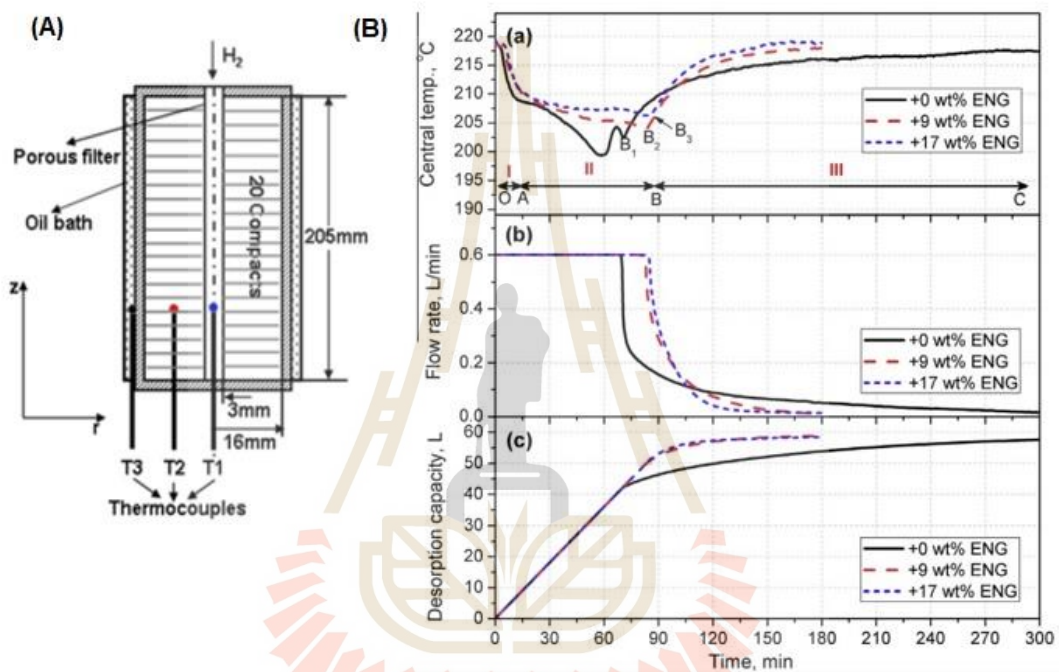
Figure 2.8 Laboratory-scale hydrogen storage tank (A) and Hydrogen desorption graph of compacted $Mg(NH_2)_2–2LiH–0.07KOH$ with different ENG contents (B).

From Figure 2.8, when ENG is added in the hydride-based tank, the diffusion pathway and heat transfer of the hydride enhance. The latter results in an improvement of the hydrogen desorption process of the tank.

To the best of our knowledge, there have been no studies on the upscaling of $LiNH_2$-LiH to hydrogen storage tanks. In this study, the powder samples of $LiNH_2$-LiH will be compacted into the pellets prior to packing into the small tank to increase volumetric hydrogen capacity. However, high compaction pressure results in poor hydrogen diffusion and poor de/rehydrogenation kinetics and reversibility. Thus, catalysts and/or additives of titanium-based catalysts (TiF_4) and multi-walled carbon nanotubes (MWCNTs) will be added into $LiNH_2$-LiH. De/rehydrogenation kinetics of compacted $LiNH_2$-LiH is favored by the catalytic properties of TiF_4 as well as the improved hydrogen diffusion and thermal properties from MWCNTs (Plerdsranoy et al., 2017).

2.4 References

Aguey-Zinsou, K.F., Yao, J., Xiao G.Z. (2007). Reaction Paths between LiNH2 and LiH with Effects of Nitrides. *J. Phys. Chem. B*, *111*, 12531-12536. doi: 10.1021/jp075002l

Amica, G., Arneodo, P., and Gennari, Larochette F.C. (2015). Hydrogen storage properties of $LiNH_2$–LiH system with MgH_2, CaH_2 and TiH_2 added. *Int. J. Hydrogen Energy, 40,* 9335-9346. doi: 10.1016/j.ijhydene.2015.05.091

Chaise, A., de Rango, P., Marty, Ph., Fruchart, D. (2010). Experimental and numerical study of a magnesium hydride tank. *Int. J. Hydrogen Energy, 35,* 6311– 6322. doi: 10.1016/j.ijhydene.2010.03.057

Chen, P., Xiong, Z., Luo, J., Lin, J., and Tan, K.L. (2002). Interaction of hydrogen with metal nitrides and imides. *Nature, 420,* 302-304. doi: 10.1038/nature01210

Chen, P., Xiong, Z., Luo, J., Lin, J., and Tan, K.L. (2003). Interaction between lithium amide and lithium hydride. *J. Phys. Chem. B, 107*, 10967-10970. doi: 10.1021/jp034149j

Chung, C.A., Yang, S.W., Yang, C.Y., Hsu C.W., and Chiu, P.Y. (2013). Experimental study on the hydrogen charge and discharge rates of metal hydride tanks using heat pipes to enhance heat transfer. *Appl. Energy, 103,* 581– 587. doi: 10.1016/j.apenergy.2012.10.024

Davies, R.A., and Anderson, P.A. (2015). Synthesis and characterization of two new amide chloride compounds: Potential H_2 storage materials. *Int. J. Hydrogen Energy, 40,* 3001-3005. doi: 10.1016/j.ijhydene.2014.12.044

Dong, B.X., Ge, J., Teng, Y.L., Gao, J.J., and Song, L. (2015). Improved dehydrogenation properties of the $LiNH_2$-LiH system by doping with alkaline metal hydroxides. *J. Mater. Chem, 3,* 905-911. doi: 10.1039/C4TA03898C

Dong, B.X., Gao, J.J., Tan, H., Teng, Y.L., Wang, L.Z., and Liu, W.L. (2016). Hydrogen desorption improvement of the $LiNH_2$-LiH-KF composite. *Int. J. Hydrogen Energy, 41,* 16122-16128. doi: 10.1016/j.ijhydene.2016.04.220

Dong, B.X., Wang, L.Z., Teng, Y.L., Li, Z.W., and Zhao, J. (2017). Superior effect of RbF on decreasing the dehydrogenation operating temperature of the LiNH$_2$-LiH system. *J. Alloys Compd, 697,* 62-67. doi: 10.1016/j.jallcom.2016.12.130

Du, L., Mauer, G., and Vaßen, R. (2015). Reaction behavior of the Li-N-H hydrogen storage system with boron nitride as an additive, *Metall. Mater. Trans, 2,* 50-57. doi: 10.1007/s40553-015-0043-z

Fernández Albanesi, L, Arneodo Larochette, P., and Gennari, F.C. (2013). Destabilization of the LiNH$_2$-LiH hydrogen storage system by aluminum incorporation. *Int. J. Hydrogen Energy, 38,* 12325-12334. doi:10.1016/j.ijhydene.2013.07.030

Franklin, E.C. (1935). The nitrogen system of compounds; Reinhold, *New York*, pp53–63.

Ichikawa, T., Hanada, N., Isobe, S., Leng, H., and Fujii, H. (2004). Mechanism of Novel Reaction from LiNH$_2$ and LiH to Li$_2$NH and H$_2$ as a Promising Hydrogen Storage System. *J. Phys. Chem. B, 108,* 7887-7892. doi: 10.1021/jp049968y

Jain, A., Agarwal, S., and Ichikawa, T. (2018). Catalytic Tuning of Sorption Kinetics of Lightweight Hydrides: A Review of the Materials and Mechanism. *Catalysts, 8,* 651. doi:10.3390/catal8120651

Jebsen, J., Milanese, C., Girella, A., Lozano, G.A., Pistidda, C., Bellosta von Colbe, J.M., Marini, A., Klassen, T., and Dornheim, M. (2013). Compaction pressure influence on materials properties and sorption behavior of LiBH$_4$- MgH$_2$ composite. *Int. J. Hydrogen Energy,* 38, 8357-8366. doi:10.1016/j.ijhydene.2013.04.090

Juza, R., and Opp, K. (1951). Metallamide und Metallnitride 25. Mitteilung. Zur Kenntnis des Lithiumimides. *Z. Anorg. Allg. Chemie, 266*, 325–330. doi: 10.1002/zaac. 19512660607

Kojima, Y., and Kawai, Y. (2005). IR characterizations of lithiumimide and amide. *Journal of Alloys and Compounds*, *395*, 236–239. doi: 10.1016/j.jallcom.2004.10.063

Klebanoff, L. (2016). Hydrogen Storage Technology Materials and Applications, International Standard Book Number-13: 978-1-4398-4108-2 (eBook - PDF).

Lin, H. J., Li, H.W., Murakami, H., and Akiba, E. (2018). Remarkably improved hydrogen storage properties of LiNH$_2$-LiH composite via the addition of CeF$_4$. *Journal of Alloys and Compounds, 735,* 1017-1022. doi: 10.1016/j.jallcom.2017.10.239

Lozano, G.A., Bellosta von Colbe, J.M., Bormann, R., Klassen, T., and Dornheim, M. (2011). Enhanced volumetric hydrogen density in sodium alanate by compaction. *J. Power Sources, 196,* 9254–9259. doi: 10.1016/j.jpowsour.2011.07.053

Markmaitree, T., Ren, R., and Shaw, L.L. (2006). Enhancement of lithium amide to lithium imide transition via mechanical activation. *The Journal of Physical Chemistry B, 110,* 20710–20718. doi: 10.1021/jp060181c

Mazzucco, A., Dornheim, M., Sloth, M., Jensen, T.R., Jensen, J.O., and Rokni, M. (2014). Bed geometries, fueling strategies and optimization of heat exchanger designs in metal hydride storage systems for automotive applications: A review. *Int. J. Hydrogen Energy, 39,* 17054–17074. doi: 10.1016/j.ijhydene.2014.08.047

Modi, P., and Aguey-Zinsou, K.F. (2021). Room Temperature Metal Hydrides for Stationary and Heat Storage Applications: A Review. *Front. Energy Res, 9,* 616115. doi: 10.3389/fenrg.2021.616115

Nayebossadri, S., Aguey-Zinsou, K.F., and Guo, Z.X. (2011). Effect of nitride additives on Li-N-H hydrogen storage system. *Int. J. Hydrogen Energy, 36,* 7920-7926. doi: 10.1016/j.ijhydene.2011.01.088

Partnership, U.S.D. (2017). Target Explanation Document: Onboard Hydrogen Storage for Light-Duty Fuel Cell Vehicles. *[On-line]. Avialable:* https://www.energy.gov/sites/prod/files/2017/05/f34/fcto_targets_onboard_hydro _storage_explanation.pdf.

Ping, C., Feng, B.Q., Ge, J., Li, G.Z., Zhu, W., Teng, Y.L., Zhang, Y.R., and Dong, B.X. (2019). Cyclic reaction-induced enhancement in the dehydrogenation performances of the KNH$_2$-doped LiNH$_2$ and LiH system. *Int. J. Hydrogen Energy, 45,* 25927-25934. doi:https:10.1016/ j.ijhydene.2019.09.109 in press.

Plerdsranoy, P., Chanthee, S., and Utke, R. (2017). Compaction of LiBH$_4$-MgH$_2$ doped with MWCNTs-TiO$_2$ for reversible hydrogen storage. *Int. J. Hydrogen Energy, 42,* 978-986. doi: 10.1016/j.ijhydene.2016.11.066

Shaw, L.L., Osborn, W., Markmaitree, T., and Wan, X. (2008). The reaction pathway and rate limiting step of dehydrogenation of the LiNH$_2$+LiH mixture. *J. Power Sources*, *177*, 500–505. doi: 10.1016/j.jpowsour.2007.11.029

Shim, J.H., Park, M., Lee, Y.H., Kim, S., Im, Y.H., Suh, J.Y., and Cho, Y.W. (2014). Effective thermal conductivity of MgH$_2$ compacts containing expanded natural graphite under a hydrogen atmosphere. *Int. J. Hydrogen Energy, 39,* 349– 355. doi: 10.1016/j.ijhydene.2013.09.092

Teng, Y.L., Ichikawa, T., and Kojima, Y. (2011). Catalytic Effect of Ti-Li-N Compounds in the Li-N-H System on Hydrogen Desorption Properties. *J. Phys. Chem. C, 115*, 589-593. doi: 10.1021/jp107313r

Titherley, A.W. (1894). XLV. – Sodium, potassium, and lithium amides. *Journal of the Chemical Society, 65,* 504-522. doi: 10.1039/CT8946500504

Varin, R.A., Jang, M., and Polanskib, M. (2010). The effects of ball milling and molar ratio of LiH on the hydrogen storage properties of nanocrystalline lithium amide and lithium hydride (LiNH$_2$ + LiH) system. *Journal of Alloys and Compounds, 491,* 658–667. doi:10.1016/j.jallcom.2009.11.035

Varin, R.A., and Jang, M. (2011). The effects of graphite on the reversible hydrogen storage of nanostructured lithium amide and lithium hydride (LiNH$_2$-1.2LiH) system. *J. Alloys Compd, 509,* 7143-7151. doi: 10.1016/j.jallcom.2011.04.036

Wu, Z., Yang, F.S., Zhang, Z.X., and Bao, Z.W. (2014). Magnesium based metal hydride reactor incorporating helical coil heat exchanger: Simulation study and optimal design. *Appl. Energy, 130,* 712–722. doi: 0.1016/j.apenergy.2013.12.071

Yan, M., Sun, F., Liu, X.P., Ye, J.H., Wang, S.M., and Jiang, L.J. (2015). Effects of graphite content and compaction pressure on hydrogen desorption properties of $Mg(NH_2)_2$–2LiH based tank. *J. Alloys Compd, 628,* 63-67. doi: 10.1016/j.jallcom.2014.12.173

Zhang, T., Isobe, S., Matsuo, M., Orimo, S.I., Wang, Y., Hashimoto, N., and Ohnuki, S. (2015). Effect of Lithium Ion Conduction on Hydrogen Desorption of $LiNH_2$-LiH Solid Composite. *ACS Catal, 5,* 1552-1555. doi: 10.1021/cs501782y

Züttle, A., and Schlapbach, L. (2008). Hydrogen as a Future Energy Carrier. WILEY-VCH Verg GmbH & Co. KGaA, Weinhein, ISBN: 978-3-527-30817-0.

CHAPTER III

EXPERIMENTAL SECTION

3.1 Chemicals

Table 3.1 Chemicals used in this work.

Chemicals	Formular	specification	Supplier
Lithium amide	$LiNH_2$	95 %	Aldrich
Lithium hydride	LiH	95 %	Aldrich
Titanium tetrafluoride	TiF_4	99 %	Acros Organics
Multiwall carbon nanotubes	MWCNTs	-	diameter of 20-50 nm, Nano Materials Research Unit

3.2 Apparatus

3.2.1 Glovebox and high-energy ball milling

Due to the sensitivity of hydride materials to air and moisture, all samples were handled under a nitrogen atmosphere in the glove box (Figure 3.1(A)). The ball milling was used for sample preparation (Figure 3.1(B)).
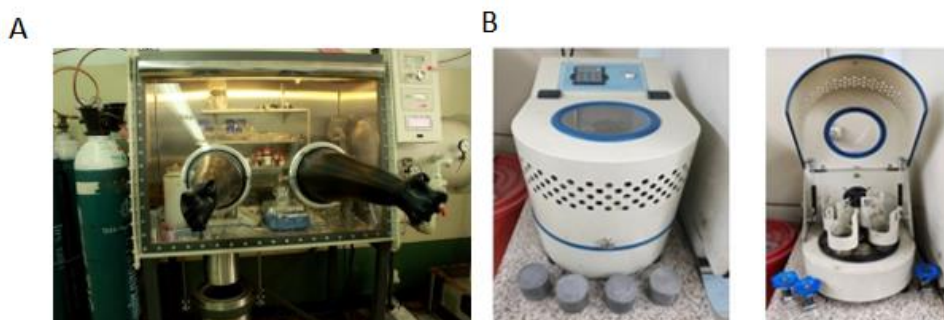

Figure 3.1 Glove box (Omni-Lab System, VAC) (A) and A QM0.4L Planetary Ball Mill, Nanjing Chishun Science & Technology (B).

3.3 Sample preparation

3.3.1 Compacted LiNH$_2$-LiH doped with TiF$_4$ and MWCNTs

LiNH$_2$ was mixed with LiH by 1:1 molar ratio and milled for 5 h and 10 h with a ball-to-powder weight ratio of 20:1 and 580 rpm, respectively, to obtain LiNH$_2$-LiH composites, denoted as LNL. LNL composite (5 h) was milled with 5.0 wt.%TiF$_4$ for 5 h and with MWCNTs for 10 min. The powder samples of LNL (10h) and LNL-TiF$_4$-MWCNTs were compressed into the pellets under 200 Mpa using a pellet die set with 15 mm diameter to obtain the compacted samples of LNL and LNL-TiF$_4$-MWCNTs, respectively. The densities of the LNL and LNL-TiF$_4$-CNT pellets were ~0.7 and 1.00 g/cm^3, respectively.

3.3.2 LiH-sandwiched LiNH$_2$-LiH-TiF$_4$-MWCNTs pellets

LiH was pre-milled for 5 h and milled with 1 wt. % MWCNTs for 30 min. The powder sample of LNL (5h) obtained from 3.3.1 was sandwiched between MWCNTs-doped LiH by compressing under 200 MPa to obtain LiH-sandwiched LNL (Figure 3.2(A)). The amounts of MWCNTs-doped LiH layers were 10, 20, and 30 wt. % with respect to LNL content, and the obtained pellet samples were named LNL-10% LiH, LNL-20% LiH, and LNL-30% LiH, respectively.

3.4 Small hydrogen storage tanks containing compacted LNL, LNL-TiF$_4$-MWCNTs and LiH-sandwiched LNL

All compacted samples (~2-3 g) were packed into separated cylindrical tanks with a packing volume of 21.7 mL (Figure 3.2(B-D)). Hydrogen diffusion inside the tank was improved by inserting the stainless-steel (SS) mesh sheets between the compacted pellets. Temperature profiles inside the tank were investigated using K-type thermocouples from SL heater (TC1, TC2, and TC3 inserted at the depths of 3, 2, and 1 cm, respectively) (Figure 3.2(C-D)).
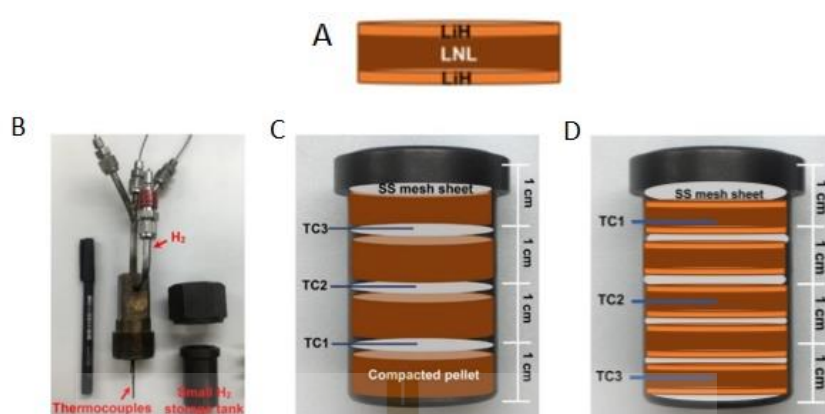
Figure 3.2 Schematic draw of LiH-sandwiched LNL pellet (A), the components of small hydrogen storage tank (B), and the positions of thermocouples along the tank length packed with compacted samples of LNL and LNL-TiF$_4$-MWCNTs (C) and LiH-sandwiched LNL (D).

3.5 Characterizations

3.5.1 Chemical compositions and structure

3.5.1.1 Powder x-ray diffraction (PXD)

Powder x-ray diffraction (PXD) experiments were done using a Bruker D8 ADVANCE with Cu Kα source (λ = 0.15406 nm). The pellet sample was ground and packed in the sample holder covered with a poly (methylmethacrylate)(PMMA) dome (Figure 3.3) under a nitrogen-filled glove box. The experiments were investigated at the 2θ range and the scanning step of 10–80° and 0.02°/s, respectively.

Figure 3.3 An airtight sample holder covered with a PMMA dome.

3.5.1.2 Fourier transform infrared spectroscopy (FTIR)

Fourier transform infrared spectroscopy (FTIR) spectra were collected using an attenuated total reflection (ATR) mode (a Bruker T27/Hyp 2000) in 4000-400 cm^{-1} wavenumber range with 64 scans (Figure 3.4).

Figure 3.4 FTIR spectrometer of Tensor 27-Hyperion 2000 (Bruker).

3.5.1.3 X-ray photoelectron spectroscopy (XPS)

X-ray photoelectron spectroscopy (XPS) experiments were carried out at the Suranaree University of Technology (SUT), National Nanotechnology Center (NANOTEC) and Synchrotron Light Research Institute (SLRI) joint research facility, Synchrotron Light Research Institute (Public organization), Thailand (Figure 3.5). A PHI5000 Versa Probe II (ULVAC-PHI Inc., Japan) with Al Kα (1.486 keV) radiation as an excitation source was used. The powder samples were deposited on the sample holder using carbon glue tape in the glove box. Prior to the measurements, the samples were placed in the high vacuum chamber (1×10^{-8} mbar) for 2 h. The high-resolution scan of each element was collected using a pass energy of 46.95 eV and a step size of 0.05 eV. Dual-beam charge neutralization (low energy electron and ion beam) method was used to minimize sample charging. The binding energy was calibrated with respect to the C 1s peak (284.8 eV).

The data was analyzed using MultiPak software version 9.6.0 (ULVAC-PHI, Japan). Peak fitting was performed after Shirley background subtraction. The symmetrical Gaussian-Lorentzian function was used to approximate the line shapes of the fitting components.

Figure 3.5 X-ray photoelectron spectroscopy at Suranaree University of Technology (SUT), National Nanotechnology Center (NANOTEC) and Synchrotron Light Research Institute (SLRI).

3.5.2 Hydrogen sorption properties

3.5.2.1 Simultaneous thermal analysis (STA) coupled with mass spectroscopy (MS)

Hydrogen desorption was characterized by differential scanning calorimetry (DSC) and thermogravimetry (TG) using a Netzsch (STA 449 F3 Jupiter) (Figure 3.8). The sample (~15 mg) was heated to 500 °C (5 °C/min) under 50 mL N_2/min. The relative signals of H_2 and NH_3 released from the sample were investigated by mass spectroscopy (MS) using a Netzsch QMS 403C (Figure 3.6).

Figure 3.6 STA 449 F3 Jupiter coupled with QMS 403C (Netzsch).

3.5.2.2 Sievert-type apparatus for tank scale

Titration measurements were carried out using a test station automatically controlled by a program created in the Labview® environment (Dansirima et al., 2019), (Thiangviriya et al., 2019), (Thongtan et al., 2018). The small hydrogen storage tanks packed with the compacted samples were assembled with other components of the sample holders for titration measurement (Figure 3.7). The direct-acting plunger solenoid valves (a Bürkert Type 0255) were used to control hydrogen consumption and liberation during de/rehydrogenation. The pressure change during the experiments was detected by a pressure transducer (0–3000 psig, an OMEGA Engineering PX309–3KGI). Temperature, pressure, and mass flow rate profiles were transferred to the computer using the module data loggers (a National Instruments NI USB-6009 and a Wisco AI210). Hydrogenation was carried out at isothermal conditions (Tset = 330 °C) under 10–15 bar H_2. Dehydrogenation was at Tset = 330 °C and began with the hydrogen pressure of 15 bar, remaining after hydrogenation. A mass flow controller (MFC, a Bronkhorst EL-FLOW selected F-201CV) with the operating range of 0–1.0 standard L/min (SLM) was used to measure the content of hydrogen desorbed.

The volume of hydrogen gas was achieved by integrating the peak area of hydrogen mass flow rate (SLM) versus time (min) plot. Total hydrogen storage capacity, defined as the combination of material hydrogen capacity and hydrogen content remaining after absorption was calculated as following equations.

$$V_{STP} \quad = \quad \frac{P_s V_s T_{STP}}{T_s P_{STP}} \tag{3.1}$$

$$n_{H_2} \quad = \quad \frac{V_{STP}}{22.4 \, L \cdot mol^{-1}} \tag{3.2}$$

$$H_2 \text{ capacity (wt. \%)} \quad = \quad \frac{n_{H_2} \times 2.016 \, g/mol}{\text{sample weight (g)}} \times 100 \tag{3.3}$$

where V_{STP} (L) and V_s (SL) are volumes of hydrogen gas at standard temperature and pressure condition (STP, T_{STP}= 273.15 K and P_{STP} = 1.0133 bar) and at the standard condition of MFC (T_s = 296.15 K and P_s = 1.0156 bar), respectively. n_{H_2} (mol) is hydrogen mole and standard molar volume is 22.4 L/mol.
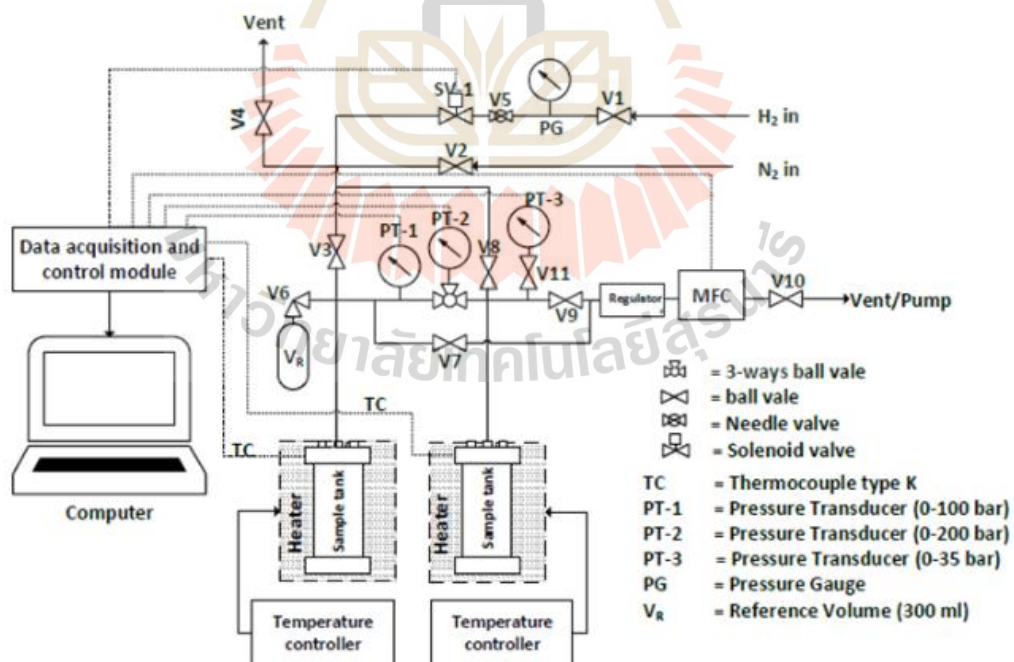

Figure 3.7 Schematic diagram of Sievert-type apparatus.

3.6 References

Dansirima, P., Thiangviriya, S., Plerdsranoy, P., Utke, O., and Utke, R. (2019). Small hydrogen storage tank filled with 2LiBH$_4$- MgH$_2$ nanoconfined in activated carbon: reaction mechanisms and performances. *Int. J. Hydrogen Energy, 44,* 10752-10762.

Thiangviriya, S., Plerdsranoy, P., Sitthiwet, C., Dansirima, P., Thongtan, P., Eiamlamai, P., Utke, O., and Utke, R. (2019). MgH$_2$-TiF$_4$-MWCNTs based hydrogen storage tank with central heat exchanger. *Int. J. Hydrog. Energy 44,* 20173–20182.

Thongtan, P., Dansirima, P., Thiangviriya,S., Thaweelap, N., Suthummapiwat, A., Plerdsranoy, P., and Utke, R. (2018). Reversible hydrogen sorption and kinetics of hydrogen storage tank based on MgH$_2$ modified by TiF$_4$ and activated carbon. *Int. J. Hydrogen Energy, 43,* 12260-12270.
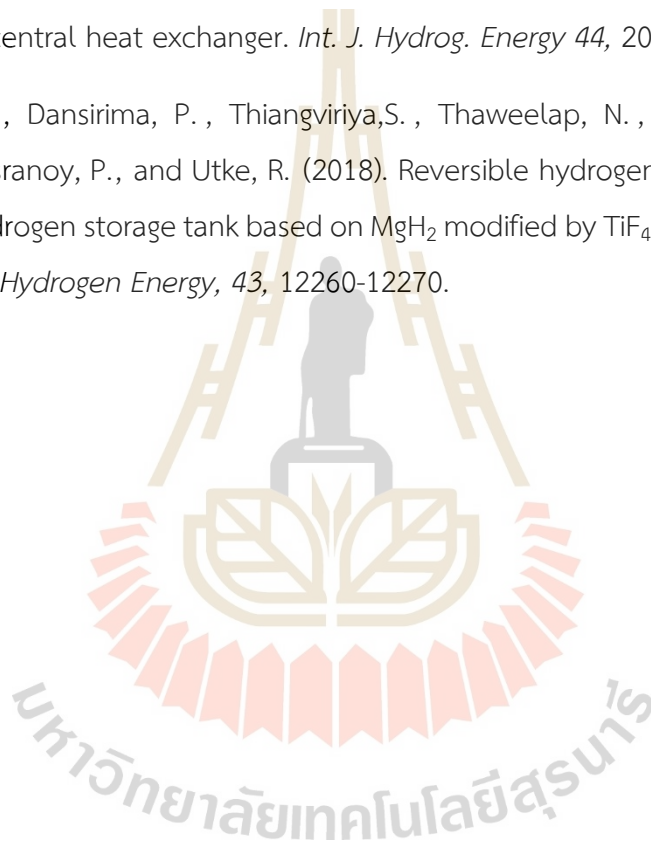
CHAPTER IV

RESULTS AND DISCUSSION

4.1 Compacted LiNH$_2$-LiH doped with TiF$_4$ and MWCNTs

Dehydrogenation of compacted samples is characterized by the simultaneous DSC-TG-MS technique. Compacted LNL shows two-step decomposition at 246 and 416 °C corresponding to H$_2$-MS signals and storage capacities of 1.7 and 4.1 wt. % H$_2$, respectively (Figure 4.1(A)).
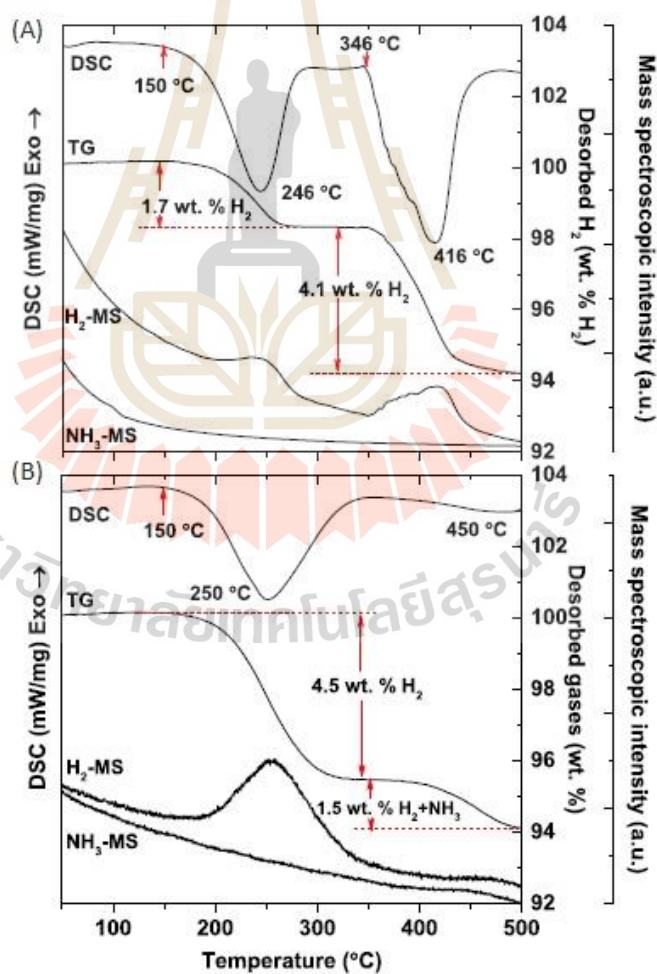

Figure 4.1 Simultaneous DSC-TG-MS results during dehydrogenation of LNL (A) and LNL-TiF$_4$-CNT (B).

From the previous reports, the decomposition of $LiNH_2$-LiH presents at 150-450 °C with NH_3 release at T > 300 °C, indicating a slow decomposition rate of $LiNH_2$ and deficient interface of NH_3 and LiH to produce Li_2NH and H_2 (Nayebossadri et al., 2011), (Dong et al., 2015), (Fernandez Albanesi et al., 2013). In this study, compacted LNL dehydrogenated at 150-450 °C without NH_3 release. This is because high compaction pressure results in a slow decomposition rate of $LiNH_2$ and poor NH_3 diffusion. In the case of compacted LNL-TiF_4-CNT, a single-step reaction shows onset and main dehydrogenation temperatures at 150 and 250 °C, respectively, with H_2 capacity of 4.5 wt. % (Figure 4.1.(B)). The theoretical capacity of LNL-TiF_4-CNT is 5.85 wt. % H_2 according to TiF_4 and MWCNTs loading contents (10 wt. %) and the theoretical capacity of $LiNH_2$-LiH (6.5 wt. % H_2). By doping with TiF_4 and MWCNTs, hydrogen content liberating from compacted $LiNH_2$-LiH at ~350 °C increases from 1.7 to 4.5 wt. % H_2 (26-77% of theoretical capacity) (Figure 4.1). Kinetic improvement can be described by the catalytic effect of TiF_4 and the enhanced hydrogen diffusion and thermal conductivity from MWCNTs (Thiangviriya et al., 2019). However, the increase of hydrogen permeability probably favors NH_3 diffusion as observed in signals of hydrogen and NH_3 (1.5 wt. %) at T > 400 °C during dehydrogenation of compacted LNL-TiF_4-CNT (Figure 4.1(B)).

Furthermore, de/rehydrogenation kinetics of these samples are investigated. Due to the signal of NH_3 detected at T > 400 °C from compacted LNL-TiF_4-CNT (Figure 4.1(B)), hydrogen desorption and absorption are carried out under isothermal at setting temperature (Tset) of ~335 °C to avoid NH_3 release. As-prepared pellets are heated from room temperature to Tset under hydrogen pressure of ~20 bar to prevent dehydrogenation. When an isothermal condition is obtained, hydrogen gas is liberated from the tank with constant flow rate of 50 standard cc/min (sccm). When dehydrogenation starts, sample temperatures reduce due to endothermic reaction. Dehydrogenation of compacted LNL tank begins at t~6 min under the system pressure (Psys) of 7.5 bar H_2 (Figure 4.2).
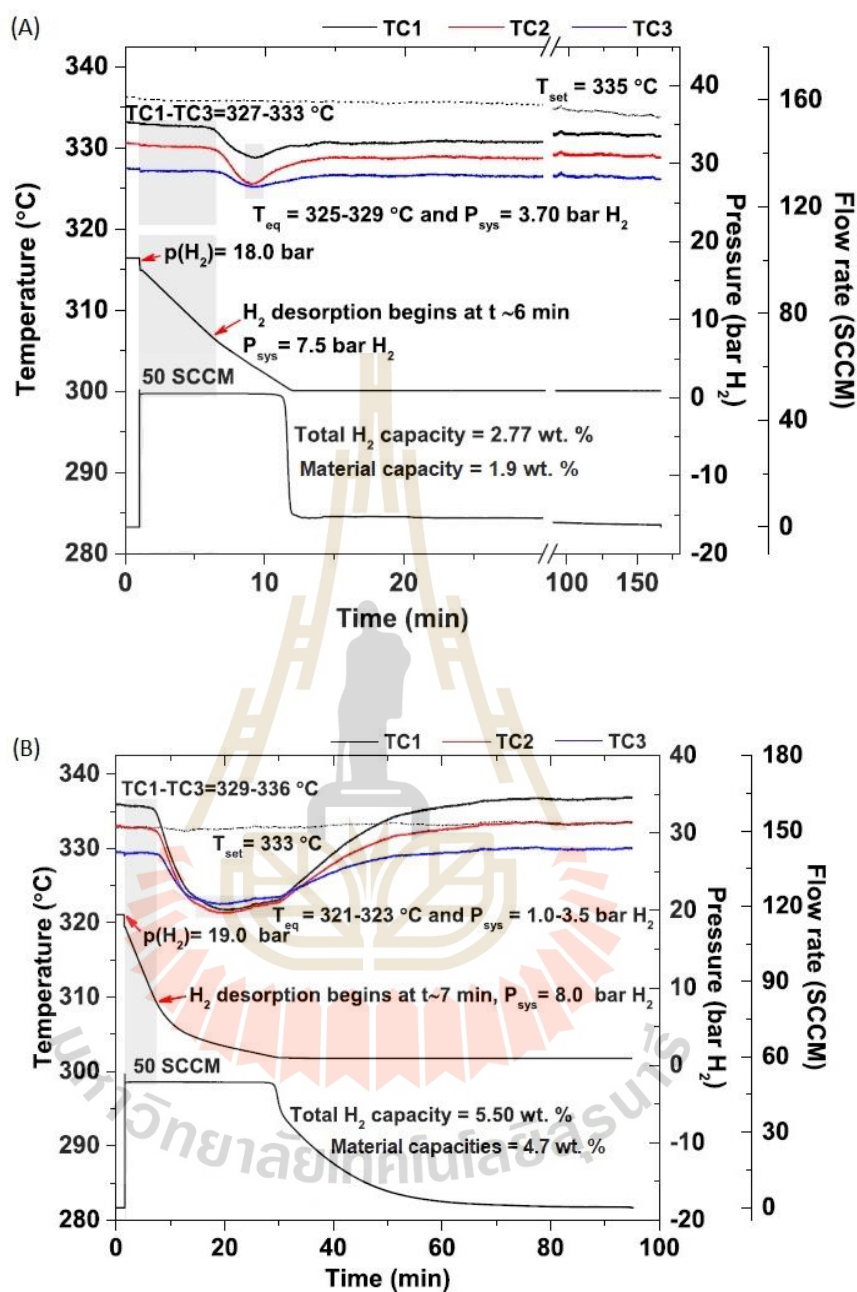
Figure 4.2 Temperature, pressure, and hydrogen flow rate profiles during dehydrogenation of small hydrogen storage tanks containing compacted LNL (A) and LNL-TiF$_4$-CNT (B).

Complete dehydrogenation is obtained with total and material storage capacities of 2.77 and 1.9 wt. % H_2, respectively. The obtained material capacity corresponds to 1.7 wt % H_2 released from the compacted LNL at T < 300 °C detected by simultaneous DSC-TG-MS result (Figure 4.1(A)). For compacted LNLTiF$_4$- CNT tank, dehydrogenation starts at t~7 min under Psys of 8.0 bar H_2 (Figure 4.2(B)). Long plateau range (~20 min) with a constant hydrogen flow rate (50 sccm) up to 30 min confirm effective desorption. Total and material hydrogen capacities of 5.50 and 4.70 wt.% H_2, respectively, agree with simultaneous DSC-TG-MS results (4.5 wt. % H_2) (Figure 4.1(B)). Therefore, the dehydrogenation kinetics of compacted was improved due to both catalytic effects of TiF_4 and hydrogen diffusion from MWCNTs. Rehydrogenation is continuously performed at isothermal conditions (Tset = 333-334 °C) under 10-20 bar H_2. When hydrogen pressure is applied to the storage tank, temperatures rise rapidly to equilibrium temperatures (Teq) of 334-347 and 359-395 °C, in agreement with equilibrium pressure (Peq) of 3.5-5 and 7-8.5 bar H_2 of compacted LNL and LNL-TiF$_4$-CNT tanks, respectively (Luo et al., 2005) (Figure 4.3).

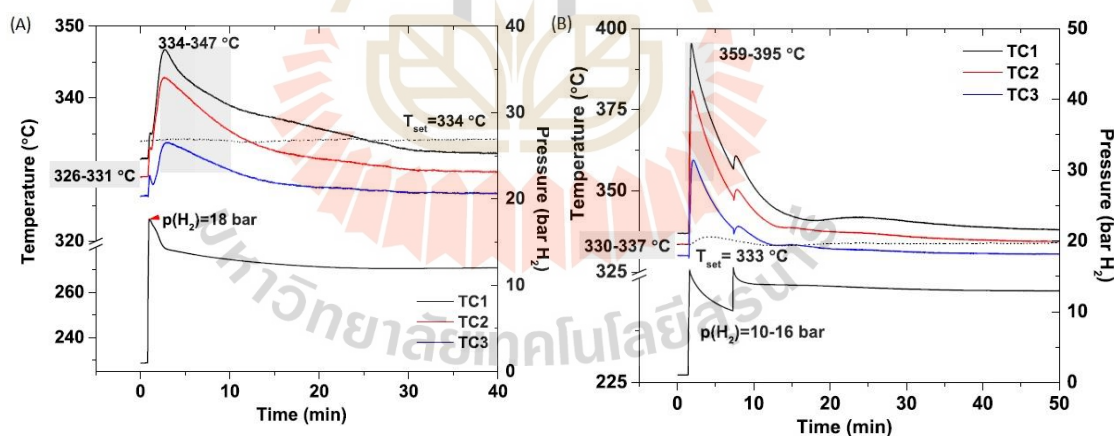**Figure 4.3** Temperature and pressure profiles during rehydrogenation of small hydrogen storage tanks containing compacted samples of LNL (A) and LNL-TiF$_4$-CNT (B).

Peq of compacted LNL-TiF$_4$-CNT is greater than that of compacted LNL and approaches the applied pressure (10-16 bar H_2), indicating superior hydrogen diffusion (Figure 4.3 (B)). The anisotropic alignment of MWCNTs in compacted LNL-TiF$_4$-CNT might provide

transporting channels for hydrogen in all directions of the compacted samples. The latter favors hydrogen diffusion during desorption rather than absorption due to hydrogen being applied from only one direction (top of the tank). In addition, initial temperatures at all positions (326-331 °C) in compacted LNL tank are lower than Tset (334 °C) (Figure 4.3(A)), whereas those of compacted LNL-TiF$_4$-CNT tank (330-337 °C) are comparable to Tset (333°C) (Figure 4.3(B)). These results confirm superior thermal conductivity of compacted LNL-TiF$_4$-CNT tank. Complete rehydrogenation of both tanks is confirmed by the reduction of temperatures to the initial values within 30 min.
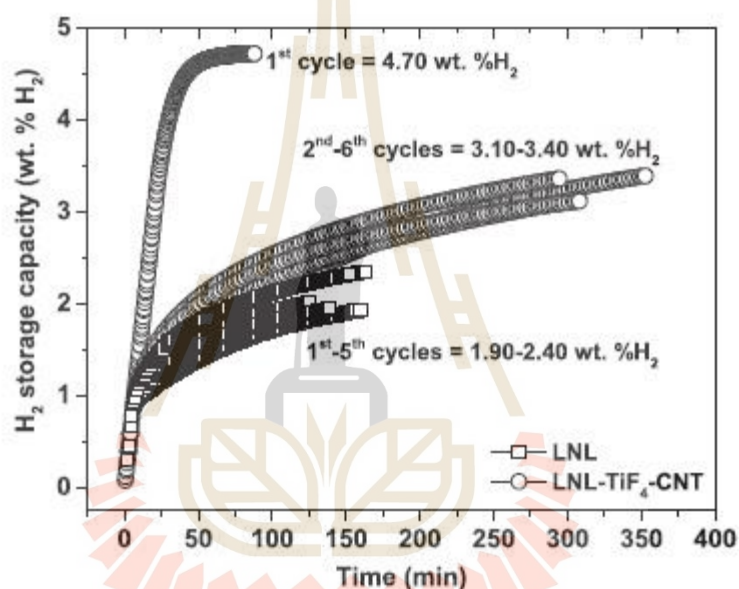
Figure 4.4 Dehydrogenation kinetics and reversibility during cycling of small hydrogen storage tanks containing compacted LNL and LNL-TiF$_4$-CNT.

Furthermore, kinetics and reversibility of compacted LNL and LNL-TiF$_4$-CNT tanks are evaluated. From Figure 4.4, (1.90-2.40 wt. % H$_2$ or 29-37% of theoretical value) are achieved from compacted LNL tank upon five hydrogen de/rehydrogenation cycles. In the case of compacted LNL-TiF$_4$-CNT tank, 4.70 wt. % H$_2$ is obtained within 100 min during the 1st cycle. However, the hydrogen capacities reduce to 3.10-3.40 wt. % H$_2$ (53-58% of theoretical value) with slower kinetics during the 2nd-6th cycles. Nevertheless, reversible hydrogen capacity increases from 37 to 58% of theoretical values after doping with TiF$_4$ and MWCNTs.

Reaction mechanisms during de/rehydrogenation of both tanks are studied by PXD and FTIR techniques. From Figure 4.5(a), as-prepared LNL reveals diffraction patterns of $LiNH_2$ and LiH, implying no reaction between hydride materials during ball milling. Upon cycling (the 1st- 2nd de/rehydrogenation), diffraction patterns of $LiNH_2$, Li_2NH, LiH, and Li_2O are observed (Figure 4.5(b-d)). For FTIR results, all samples show vibrational peaks of $LiNH_2$ at 3314 and 3259 cm^{-1}, while de/rehydrogenated pellets show the signal of Li_2NH at 3252 and 3184 cm^{-1}, corresponding to asymmetric and symmetric stretching of N-H bonds, respectively (Figure 4.6(a-d)) (Kojima et al., 2005). The signals of $LiNH_2$, Li_2NH, and LiH detected in de/rehydrogenated pellets hint at incomplete hydrogen desorption and poor reversibility of compacted LNL tank, in agreement with the inferior hydrogen content released and reproduced to theoretical value during cycling (Figure 4.4). The formation of Li_2O is due to oxidation of Li-containing phases with oxygen and/or humidity during sample preparation.
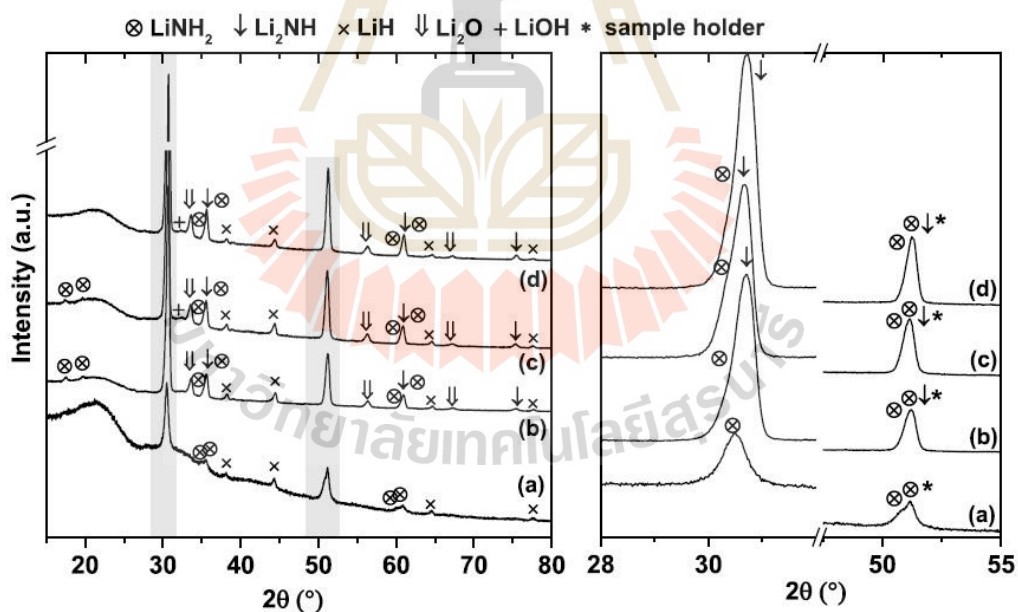

Figure 4.5 PXD spectra of as-prepared (a), dehydrogenated (b), rehydrogenated (c), and the 2nd dehydrogenated (d) samples of compacted LNL located at the middle of the tank (TC2).

In the case of compacted LNL-TiF$_4$-CNT, as-prepared powder sample shows the diffraction peaks of LiNH$_2$, LiH, and unknown phase (Figure 4.7(a)). When the reaction occurred, dehydrogenated pellet reveals characteristic peaks of Li$_2$NH and LiF (Figure 4.7(b)), hinting at complete dehydrogenation and reaction between TiF$_4$ and Li-containing phases, respectively.

Figure 4.6 FTIR spectra of as-prepared (a), dehydrogenated (b), rehydrogenated (c), and the 2nd dehydrogenated (d) samples of compacted LNL located at the middle of the tank (TC2).

Li$_2$O and LiOH signals are described by the oxidation/hydrolysis of Li-containing phases during the experiments. After rehydrogenation, not only LiNH$_2$ and LiH are reproduced but also Li$_5$TiN$_3$ and unknown phases (Figure 4.7(c)). From the previous results, Li$_5$TiN$_3$ formed by nanocontact between LiNH$_2$ and Ti could absorb excess NH$_3$ to form Li$_5$TiN$_3$(NH$_3$)$_x$, acting as a catalyst to enhance hydrogen desorption properties of Li-N-H

system (Teng et al., 2011). This phase favored desorption kinetics and reversibility of compacted LNL-TiF$_4$-CNT tank as compared with compacted LNL (Figure 4.4).

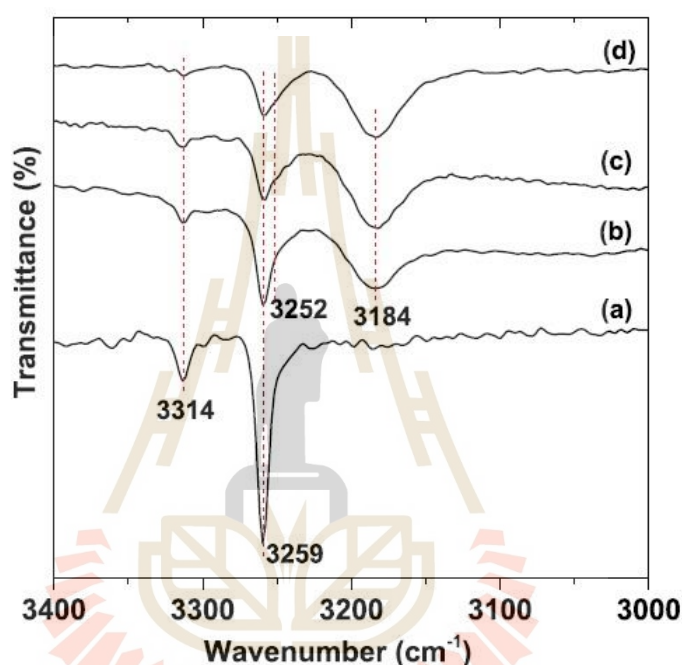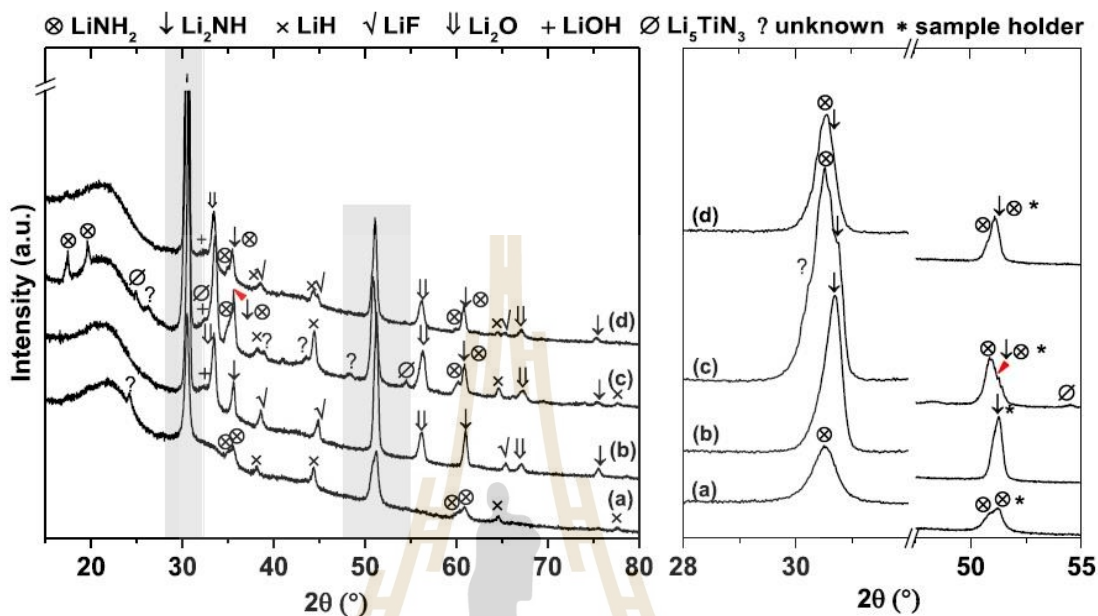**Figure 4.7** PXD spectra of as-prepared (a), dehydrogenated (b), rehydrogenated (c), and the 2nd dehydrogenated (d) samples of compacted LNL-TiF$_4$-CNT located at the middle of the tank (TC2).

For the 2nd desorption, diffraction patterns of LiNH$_2$ and LiH are recovered together with Li$_2$NH, LiF, Li$_2$O, and LiOH (Figure 4.7(d)). FTIR spectrum of as-prepared sample shows the characteristic vibrations of LiNH$_2$ (3314 and 3258 cm^{-1}) and Li$_2$NH (3252 and 3184 cm^{-1}) (Figure 4.8 (a-d)). For the dehydrogenated and rehydrogenated samples, the vibration of Li$_2$NH (Figure 4.8(b)) and LiNH$_2$ (Figure 4.8(c)) are observed, respectively. Thus, compacted LNL-TiF$_4$-CNT not only decomposes completely but also can be reversible. However, incomplete dehydrogenation during the 2nd cycle is confirmed by mixed vibrational peaks of LiNH$_2$ and Li$_2$NH (Figure 4.8(d)). This leads to the reduction of hydrogen capacity during the 2nd- 6th with respect to the 1st cycle of compacted LNL-TiF$_4$-CNT tank.
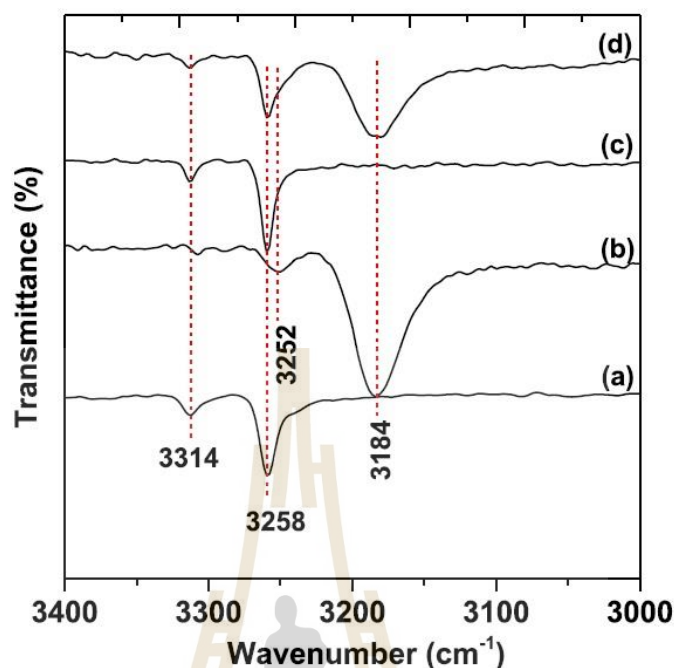
Figure 4.8 FTIR spectra of as-prepared (a), dehydrogenated (b), rehydrogenated (c), and the 2ⁿᵈ dehydrogenated (d) samples of compacted LNL-TiF₄-CNT located at the middle of the tank (TC2).

De/rehydrogenation performances at different positions (TC1-TC3) inside the compacted LNL-TiF₄-CNT tank are investigated. As-prepared powder showed the vibrational peaks of LiNH₂ (3314 and 3260 cm⁻¹) and Li₂NH (3250 and 3180 cm⁻¹). For dehydrogenated samples, all positions present mainly the vibration of Li₂NH with slight signal of LiNH₂ Figure 4.9. Therefore, reaction rate and mechanisms inside the compacted LNL-TiF₄-CNT tank are comparable. Moreover, the expansion/contraction of the pellet sample upon de/rehydrogenation cycles results in the deformation and/or cracks (Figure 4.10). It should be noted that both LNL and LNL-TiF₄-CNT show good mechanical stability upon cycling.
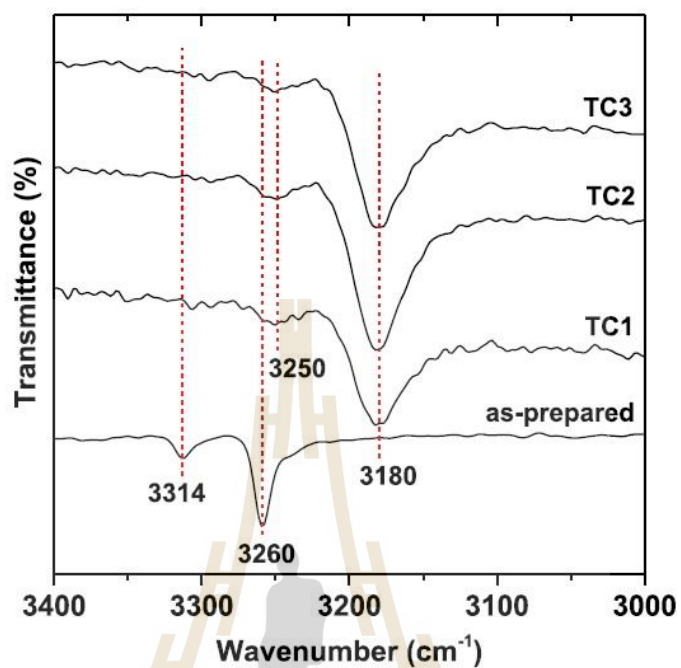
Figure 4.9 FTIR spectra of as-prepared and dehydrogenated samples at different positions inside the tank containing compacted LNL-TiF$_4$-CNT.
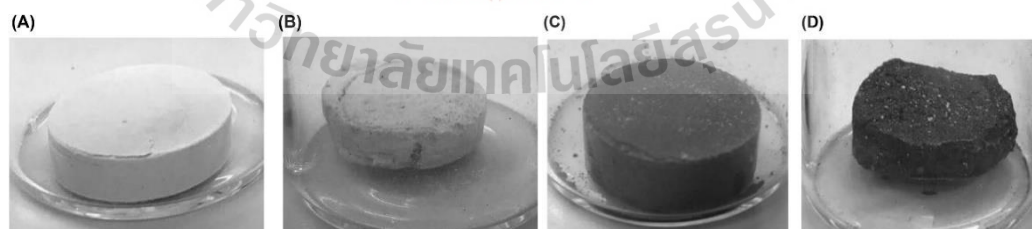

Figure 4.10 Pictures of compacted LNL and LNL-TiF$_4$-CNT at as-prepared state (A and C, respectively) and after cycling (B and D, respectively).

4.2 LiH-sandwiched LiNH$_2$-LiH-TiF$_4$-MWCNTs pellets

From the previous work, NH$_3$ emission upon cycling might still occur due to pellet deformation (Figure 4.10). In this study, we would like to propose the idea of sandwiching LiNH$_2$-LiH with LiH layers to prevent NH$_3$ emission during de/rehydrogenation cycles. To enhance hydrogen sorption kinetics and gas diffusion, TiF$_4$ and MWCNTs are added into the middle layer of LiNH$_2$-LiH, while the outer layers of LiH are doped with 1 wt. % MWCNTs. The pellets of LiH-sandwiched LiNH$_2$-LiH contain 10–30 wt. % of MWCNTs-doped LiH layers. Dehydrogenation kinetics, reversibility, and hydrogen exchange reactions as well as the suppression of NH$_3$ release upon cycling of the LiH-sandwiched LiNH$_2$-LiH pellets are investigated. The decompositions of as-prepared LNL and LiH-sandwiched LNL pellets are characterized by simultaneous DSC-TG-MS technique as shown in Figure 4.11. All pellet samples reveal comparable onset desorption temperatures at about 200 ºC. LNL pellet shows two-step dehydrogenation at 260 and 484 ºC together with NH$_3$ release during the second step. In the case of LiH-sandwiched LNL pellets, single-step dehydrogenation at 260–262 ºC with no sign of NH$_3$ release are observed. For the percent weight loss, LNL pellet represents the combination of H$_2$ and NH$_3$ release (6.83 wt. %), while LiH-sandwiched LNL pellets liberate only H$_2$ (4.12–5.00 wt. %) (Figure 4.11). Considering comparable desorption temperatures of all LiH-sandwiched LNL pellets, the different amounts of MWCNTs-doped LiH layers (10–30 wt. %) sandwiching at both sides of LNL pellet do not affect the desorption temperature of LiNH$_2$-LiH composite during the first dehydrogenation. However, high content of MWCNTs-doped LiH content (30 wt. %) results in deficient hydrogen capacity of LNL-30% LiH (3.50 wt. %) with respect to other LiH-sandwiched LNL samples.
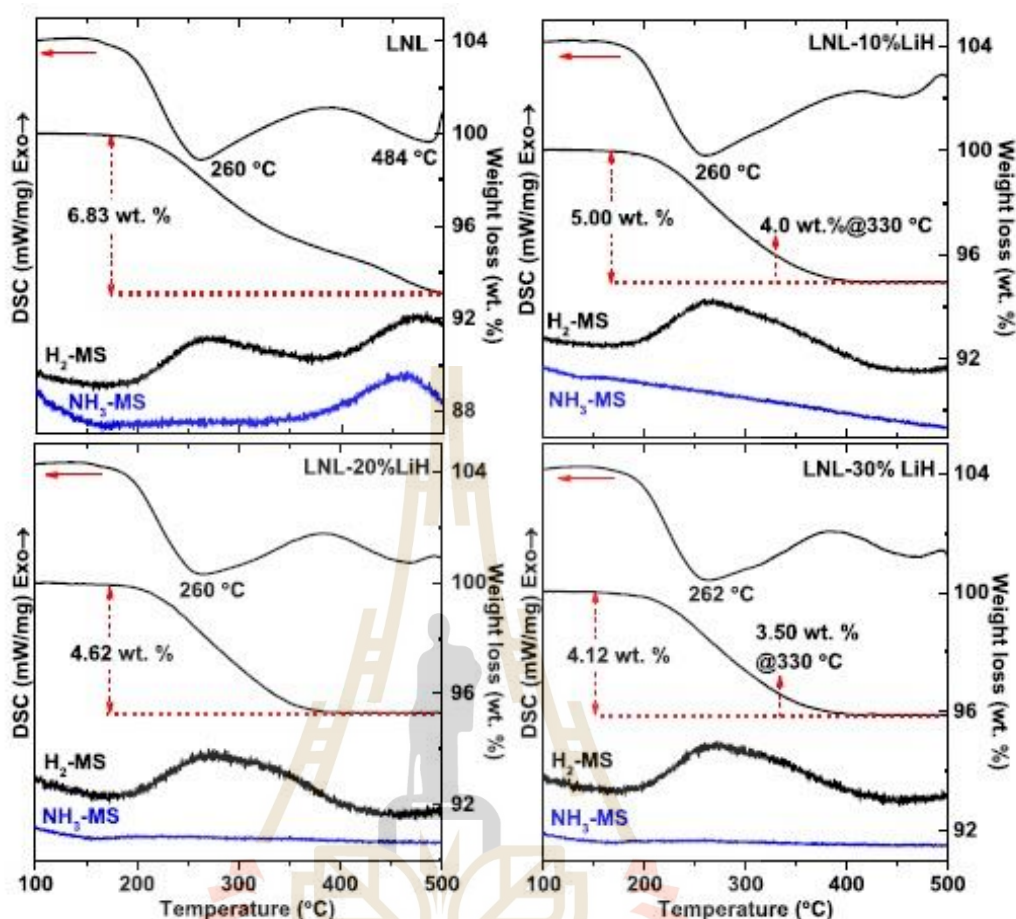
Figure 4.11 Simultaneous DSC-TG-MS results of LNL, LNL-10% LiH, LNL-20% LiH, and LNL-30% LiH pellets.

Since the dehydrogenation character of LNL-20%LiH is in between those of LNL-10% LiH and LNL-30% LiH. Further studies based on dehydrogenation kinetics, reversibility, and suppression of NH_3 release focus on the pellet samples with the lowest and the highest contents of MWCNTs-doped LiH (LNL-10% LiH and LNL-30% LiH). From Figure 4.12, total and material hydrogen capacities during the 1st cycle of LNL-10% LiH pellet are 4.97 and 3.90 wt. % H_2, respectively, while those of LNL-30% LiH pellet are 4.27 and 3.67 wt.% H_2, respectively. These agree with simultaneous DCS-TG-MS results at 330 °C (4.0 and 3.50 wt. % H_2, respectively) (Figure 4.11). Both LiH-sandwiched LNL pellets are rehydrogenated under 10-15 bar, which two-step exothermic reaction are observed at all positions (TC1-TC3) (Figure 4.13).
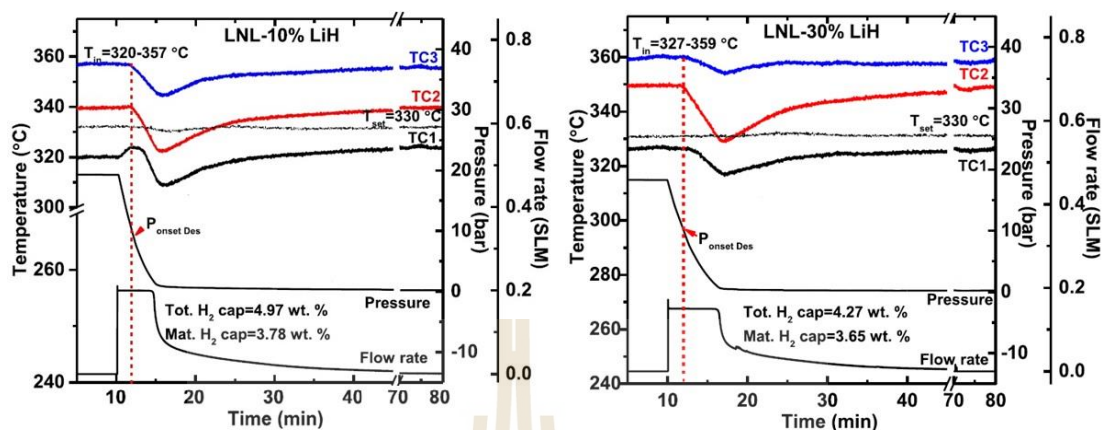
Figure 4.12 Dehydrogenation kinetics of LNL-10% LiH and LNL-30% LiH pellets.

Considering reversibility, 3.90 and 3.67 wt. % H_2 are observed during the 1st cycle of LNL-10% LiH and LNL-30% LiH, respectively (Figure 4.14). During the 2nd-6th cycles, comparable total and material capacities in the ranges of 2.9–3.3 and 2.3–2.6 wt. % H_2, respectively, are obtained from LNL-10% LiH and LNL-30% LiH, respectively.

Figure 4.13 Rehydrogenation kinetics of LNL-10% LiH and LNL-30% LiH pellets.

Figure 4.14 Dehydrogenation kinetics and reversibility of LNL-10% LiH and LNL-30% LiH pellets.

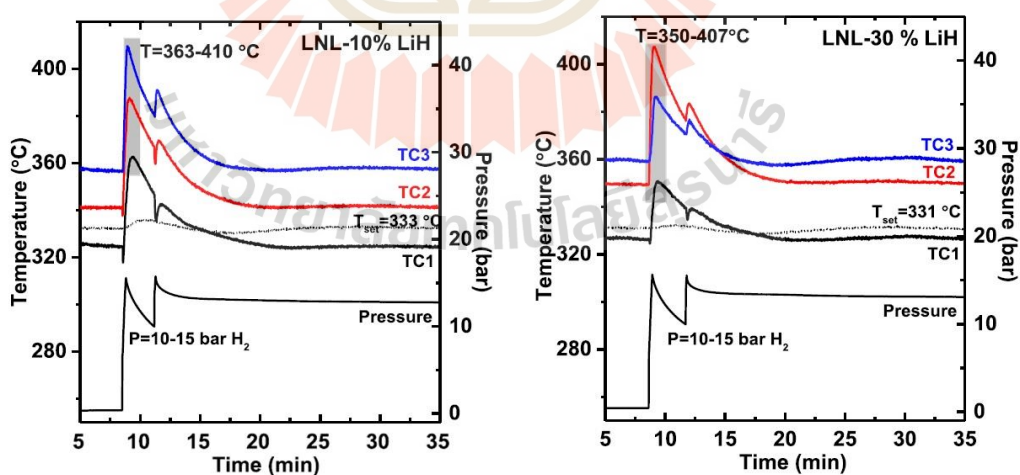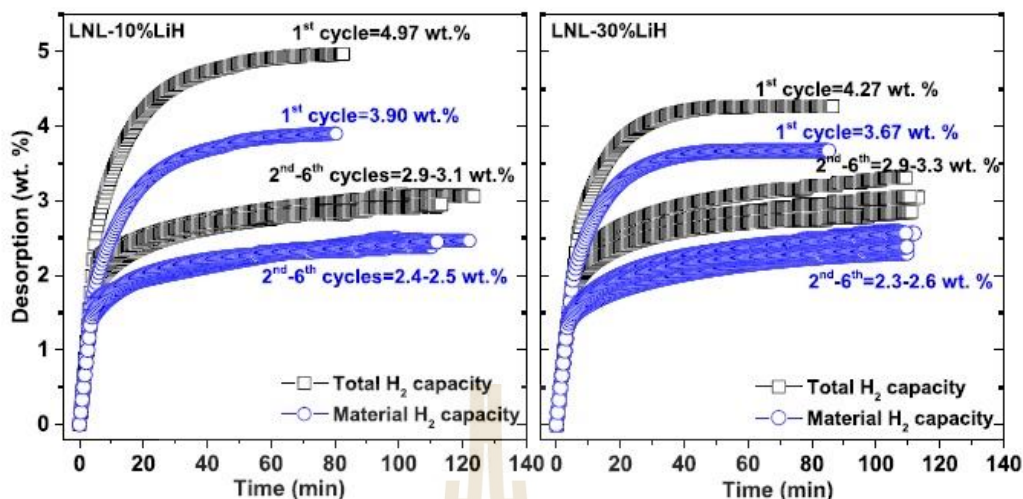After cycling, the 6th rehydrogenated pellets of both LiH-sandwiched LNL samples are investigated by simultaneous DSC-TG-MS technique to confirm NH_3 suppression. Both pellet samples reveal two-step decomposition (Figure 4.15). LNL-10% LiH releases both H_2 and NH_3 at the same temperature ranges at ~250 and 400 °C, resulting in total weight loss of 8.20 wt. % (Figure 4.15(A)). While LNL-30% LiH provides only H_2-MS signal at the same temperature together with the total capacity of 4.10 wt. % H_2 (Figure 4.15(B)). LNL-10% LiH and LNL-30% LiH pellets present percent weight losses of 2.40 and 2.10 wt. %, respectively at 330 °C, approaching the contents of gases desorbed during the 2nd-6th cycles (2.3–2.6 wt. %) (Figure 4.14). Superior dehydrogenation performance upon cycling of LNL-30% LiH to LNL-10% LiH pellet can be described by the effective suppression of NH_3 release due to sufficient LiH content and mechanical stability upon cycling of LiH layer. Figure 4.16(A) shows that LNL-10% LiH pellet with the thin layers of MWCNTs-doped LiH has some defects and/or cracks on the MWCNTs-doped LiH layer after cycling, resulting in NH_3 release (Figure 4.16(A)).
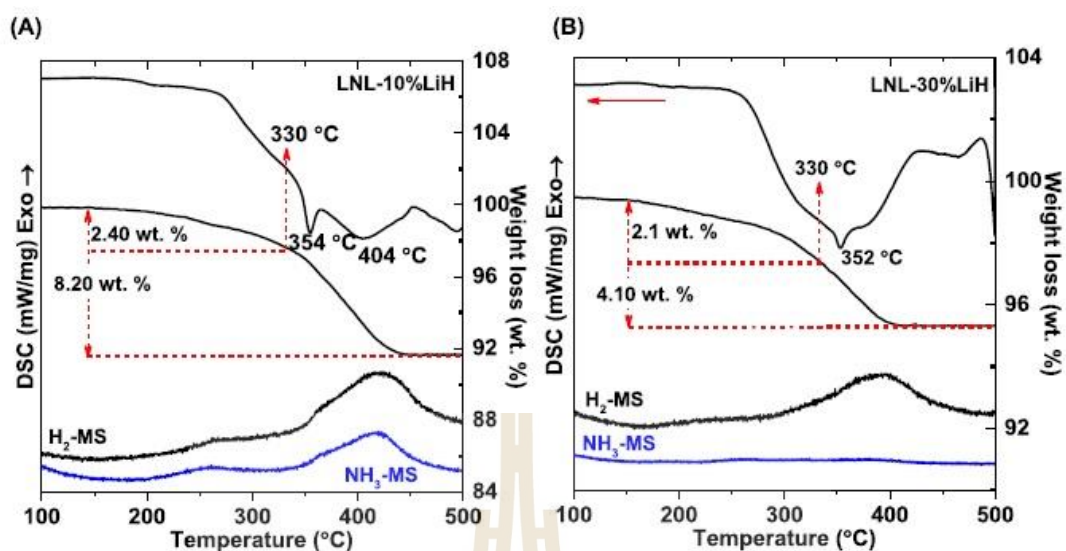
Figure 4.15 Simultaneous DSC-TG-MS results of the 6th rehydrogenated pellets of LNL-10% LiH (A) and LNL-30% LiH (B).

In the case of LNL- 30% LiH, the dense pellet of LNL layer is sandwiched with the thick layers of MWCNTs-doped LiH (Figure 4.16(B)), leading to suppression of NH_3 release upon cycling. Furthermore, chemical compositions of as-prepared, dehydrogenated, and rehydrogenated states of both LiH-sandwiched LNL samples are characterized by PXD, FTIR, and XPS techniques. Due to comparable dehydrogenation kinetics during the 2nd-6th cycles, the 6th de/rehydrogenated pellets are selected to represent the hydrogen exchange reaction upon cycling. PXD pattern of as-prepared LNL-10% LiH pellet shows the diffractions pattern of $LiNH_2$, LiH, Li_2O, and $LiTi_2O_4$, while the 5th dehydrogenated sample reveals the signals of Li_2NH, LiH, Li_2O, and $LiTi_2O_4$ (Figure 4.17(A)(a-b)). For after the 6th rehydrogenation, the diffraction peaks of $LiNH_2$ and Li_5TiN_3 are observed together with other phases, similar to as-prepared and dehydrogenated samples (LiH, Li_2O, and $LiTi_2O_4$) (Figure 4.17(A)(c)).
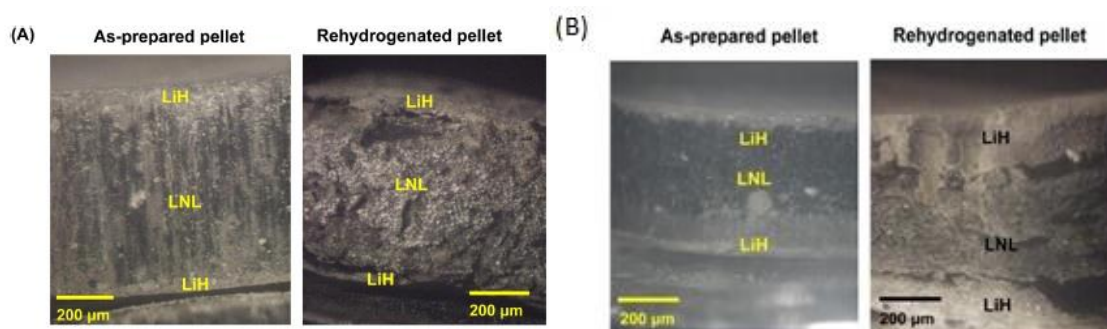
Figure 4.16 Microscope images of as-prepared and the 6th rehydrogenated pellets of LNL-10% LiH (A) and LNL-30% LiH (B).

Considering the FTIR spectra, as-prepared and the 6th rehydrogenated samples show vibrational peaks of $LiNH_2$ at 3314 and 3260 cm^{-1} (Figure 4.17(B)(c)). For the 5th dehydrogenated sample, the vibration of Li_2NH at 3252 and 3183 cm^{-1} is observed in Figure 4.17(B)(b)). The excess of LiH from the MWCNT-doped LiH layers leads to the formation of $LiTi_2O_4$. Zhang et al. (2015) proposed that $LiTi_2O_4$ could enhance the mobility of Li+ ions between LiH and $LiNH_2$ solid phases, improving dehydrogenation of the $LiNH_2$-LiH composites. Besides, Li_5TiN_3 obtained from the nanocontact between $LiNH_2$ and Ti (from TiF_4) could absorb the excess NH_3 to form $Li_5TiN_3(NH_3)_x$, acting as a catalyst for enhancing hydrogen desorption properties. Thus, these formations of several irreversible phases of Li_2O, $LiTi_2O_4$, and Li_5TiN_3 phases affect the reduction of gas content upon cycling. For the sample of LNL-30% LiH, as-prepared pellet shows the diffractions pattern of $LiNH_2$ and LiH (Figure 4.18(A)(a)), while the 5th dehydrogenated pellet reveals the signals of Li_2NH^*, Li_2O, LiH, and LiF together with $LiH_{1-x}F_x$, which the diffraction is in between those of LiH and LiF (Figure 4.18(A)(b)). The formation of $LiH_{1-x}F_x$ is in accordance with the confirmed reaction between NaH and NaF to form $NaH_{1-x}F_x$, which the diffractions of $NaH_{1-x}F_x$ located between those of NaH and NaF (Humphries et al., 2016).

Figure 4.17 PXD patterns (A) and FTIR spectra (B) of the pellets at as-prepared (a), the 5th dehydrogenated (b), and the 6th rehydrogenated (c) states of LNL-10%LiH.

In the PXD result, diffraction peaks of Li$_2$NH* are slightly shifted to lower 2θ (~0.1°) with respect to Li$_2$NH (Figure 4.18(A)(b)). This indicates that the enlargement of Li$_2$NH unit cell is probably due to the substitution of F atoms for H in Li$_2$NH structure to form

$Li_2NH_{1-y}F_y$ upon cycling, identical to the formation of $LiH_{1-x}F_x$ (Figure 4.18(A)(b)). For the sample of the 6th rehydrogenation, the characteristic peaks of $LiNH_2$, $LiTi_2O_4$, LiH, and unknown phase are observed (Figure 4.18(A)(c)), indicating the successful reversibility of the $LiNH_2$-LiH composite.
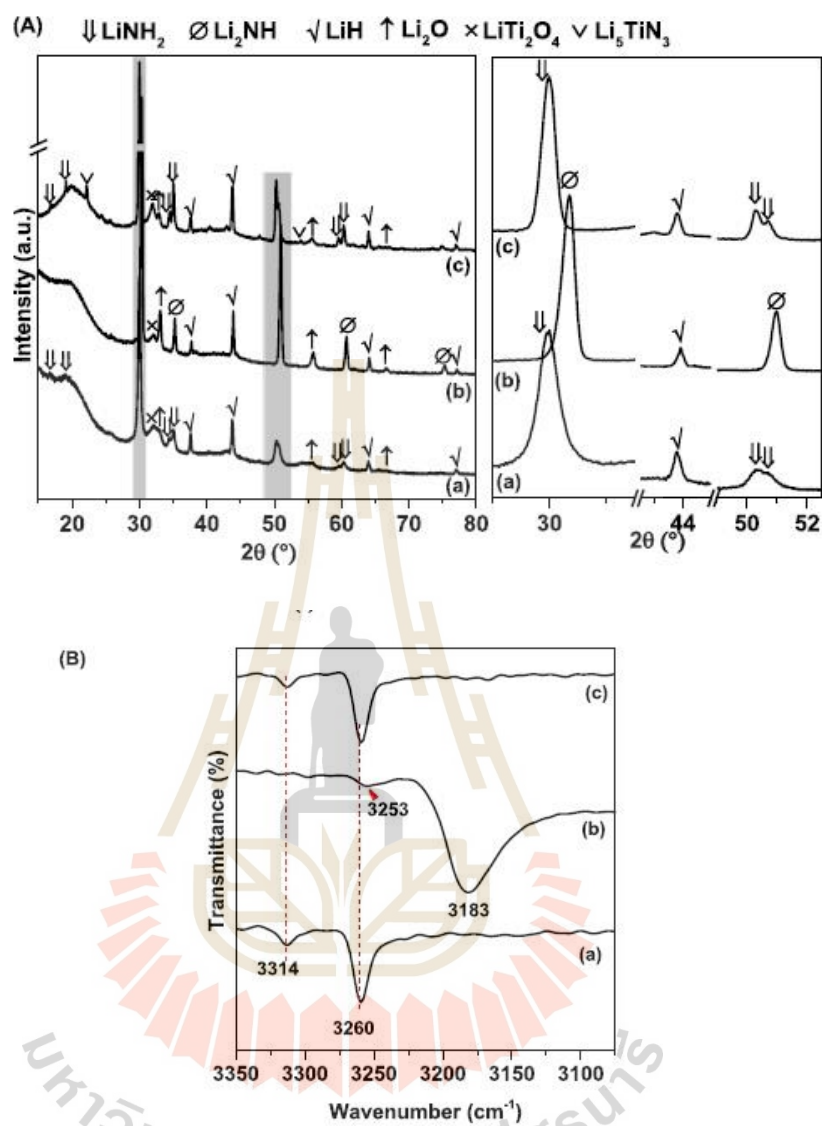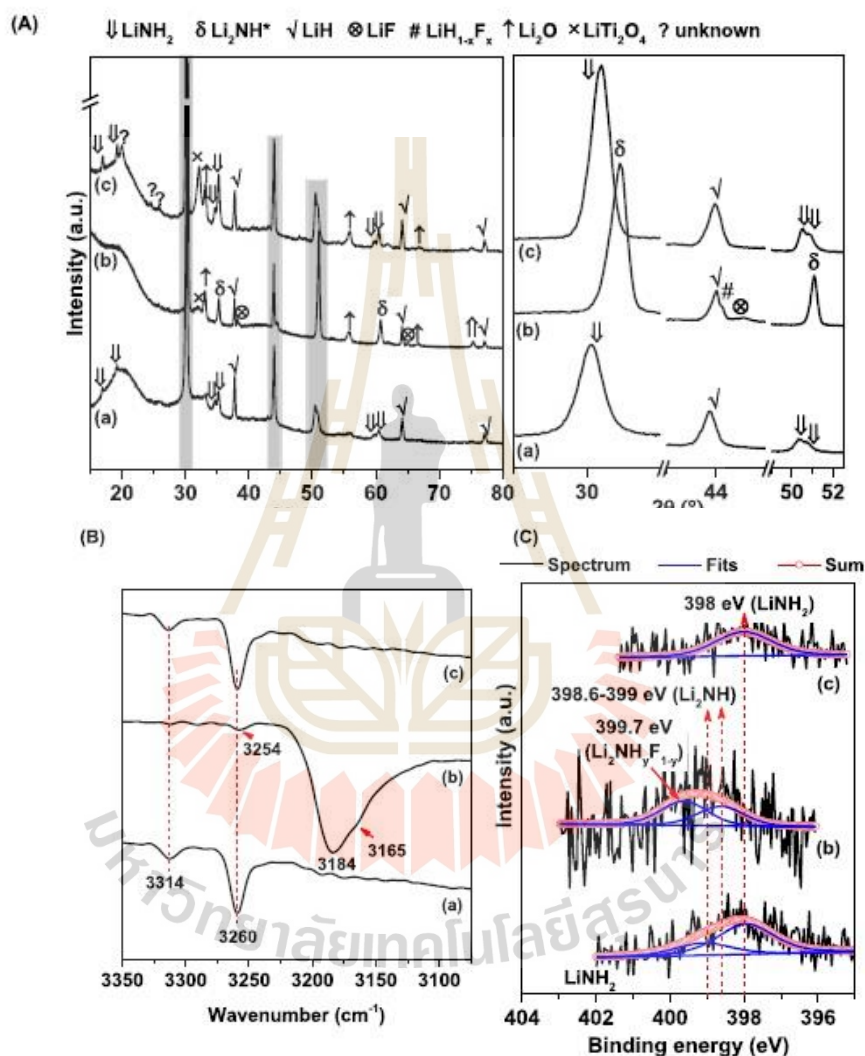

Figure 4.18 PXD patterns (A), FTIR spectra (B), and N 1s XPS spectra (C) of the pellets as prepared (a), the 5th dehydrogenated (b), and the 6th rehydrogenated (c) states of LNL-30% LiH and as-milled $LiNH_2$ powder samples.

FTIR spectra of as-prepared and the 6th rehydrogenated LNL-30%LiH also show comparable vibrations with those of LNL-10%LiH (Figure 4.18(B)(a) and (c)), i.e., asymmetric and symmetric N-H stretching of LiNH$_2$ at 3314 and 3260 cm^{-1}, respectively (Figure 4.18(B)(a) and (c)) (Kojima et al., 2005). However, the 5th dehydrogenated LNL-30% LiH shows not only characteristic peaks of Li$_2$NH at 3254 and 3184 cm^{-1} but also a shoulder peak at the lower wavenumber of 3165 cm^{-1} (Figure 4.18(B)(b)). This indicates that another N-H bond of Li$_2$NH with the enhanced bond length is probably attributed to the increase of electronegativity of the neighboring atom (F atom). This suggests that fluorine may substitute for hydrogen in Li$_2$NH to produce Li$_2$NH$_{1-y}$F$_y$, corresponding to PXD result. Furthermore, XPS experiments are conducted to confirm the formation of Li$_2$NH$_{1-y}$F$_y$. From Figure 4.18(C), N 1s XPS spectrum of as-milled LiNH$_2$ shows the characteristic peak of LiNH$_2$ and Li$_2$NH at 398 and 398.6 eV, respectively. The appearance of Li$_2$NH in as-milled LiNH$_2$ can be due to the partial decomposition of LiNH$_2$ during the milling process. For the 5th dehydrogenated pellet, signals of Li$_2$NH at ∼399 eV together with the peak at higher binding energy at 399.7 eV are observed (Figure 4.18(C)(b)). Chemical bonding with a more electronegative atom leads to the decrease of the electron density in the valence shell of N atom, resulting in the enhanced binding of the N 1s orbital. Therefore, the N 1s XPS peak at higher binding energy (399.7 eV) with respect to that of N-H bond likely belonging to Li$_2$NH (399 eV) indicates the bonding between N and electronegative atom (i.e., N-F bond in this study). This fluorine substitution of hydride materials is possible due to the comparable ionic size of the hydride and fluoride ions as well as the structural similarity of their compounds (Humphries et al., 2016), (Messer, 1970). Thus, LNL-30%LiH provides not only sufficient LiH content to consume NH$_3$ but also the formation of new reactive phases of LiH$_{1-x}$F$_x$ and Li$_2$NH$_{1-y}$F$_y$ upon cycling. This leads to positive effects on de/rehydrogenation kinetics and reversibility of LiNH$_2$-LiH, which is confirmed by hydrogen contents reproduced upon cycling and the reaction mechanisms of F-substituted phases on kinetic properties.

4.3 References

Davies, R.A., and Anderson, P.A. (2015). Synthesis and characterization of two new amide chloride compounds: potential H_2 storage materials. *Int. J. Hydrogen Energy, 40,* 3001–3005.

Dong, B.X., Ge, J,. Teng, Y.L., Gao, J.J., and Song, L. (2015) Improved dehydrogenation properties of the $LiNH_2$-LiH system by doping with alkaline metal hydroxides. *J. Mater. Chem, 3,* 905-911.

Fernandez Albanesi, L., Arneodo Larochette, P., and Gennari, F.C. (2013). Destabilization of the $LiNH_2$-LiH hydrogen storage system by aluminum incorporation. *Int. J. Hydrogen Energy, 38,* 12325-12334.

Humphries, T.D., Sheppard, D.A., Rowles, M.R., Sofianos, M.V., and Buckley, C.E. (2016). Fluorine substitution in sodium hydride for thermal energy storage applications. *J. Mater. Chem. A, 4,* 12170–12178.

Kojima,Y., and Kawai, Y. (2005). IR characterizations of lithium imide and amide. *J. Alloys Compd, 395,* 236-239.

Luo, W., and R€onnebro, E. (2005) Towards a viable hydrogen storage system for transportation application. *J. Alloys Compd, 404-406,* 392-395.

Messer, C.E. (1970). Hydrides versus fluorides: structural comparisons. *J. Solid State Chem, 2,* 144–155.

Nayebossadri, S., Aguey-Zinsou, K.F., and Guo, Z.X. (2011). Effect of nitride additives on Li-N-H hydrogen storage system. *Int. J. Hydrogen Energy, 36,* 7920-7926.

Teng, Y.L. Ichikawa, T., and Kojima, Y. (2011). Catalytic effects of Ti-Li-N compounds in the Li-N-H system on hydrogen desorption properties. *J. Phys. Chem. C, 115,* 589-593.

Thiangviriya, S., Sitthiwet, C., Plerdsranoy, P., Capurso, G., Pistidda, C., Utke, O., Dornheim, M., Klassen, T., and Utke, R. (2019). Hydrogen sorption kinetics, hydrogen permeability, and thermal properties of compacted $2LiBH_4$-MgH_2 doped with activated carbon nanofibers. *Int. J. Hydrogen Energy, 44,* 15218-15227.

Zhang, T., Isobe, S., Matsuo, M., Orimo, S.I., Wang, Y., Hashimoto, N., and Ohnuki, S. (2015). Effect of lithium ion conduction on hydrogen desorption of $LiNH_2$-LiH solid composite. *ACS Catal, 5,* 1552–1555.

CHAPTER V

CONCLUSIONS

De/rehydrogenation performances, kinetics, and reaction mechanisms of small hydrogen storage tank containing compacted $LiNH_2$-LiH doped with TiF_4 and MWCNTs were investigated. The enhanced dehydrogenation kinetics was confirmed by the alteration of reaction pathway at lower temperature range of 150-350 $^{\circ}C$. Moreover, hydrogen content released and reproduced at isothermal condition (Tset = 335 $^{\circ}C$) increased from 1.90-2.40 to 3.10-4.70 wt. % H_2. Effective dehydrogenation was confirmed by the prolonged plateau temperature range and constant hydrogen flow rate (50 sccm). Upon cycling, Li_3TiN_5 obtained from the nanocontact between $LiNH_2$ and Ti absorbed NH_3 to produce $Li_5TiN_3(NH_3)_x$, acting as catalyst for Li-N-H system. To further reduce NH_3 emission upon cycling, the composite of $LiNH_2$-LiH doped with TiF_4-MWCNTs was sandwiched with MWCNTs-doped LiH layers (10–30 wt. %). During the first dehydrogenation, compacted $LiNH_2$-LiH released NH_3 along with H_2, while LiH-sandwiched $LiNH_2$-LiH pellets desorbed hydrogen without NH_3. Kinetic properties of the 1st de/rehydrogenation of LiH- sandwiched $LiNH_2$-LiH pellets (10 and 30 wt. % MWCNTs-doped LiH) were comparable (3.5–4.0 wt. % H_2 within 60 min). Upon the 2nd-6th cycles, the gases desorbed from the pellet samples with 10 and 30 wt. % MWCNTs-doped LiH (2.3–2.6 wt. %) were mixed H_2+NH_3 and only H_2, respectively. Deficient reversible hydrogen contents were described by the formation of irreversible phases (Li_2O, $LiTi_2O_4$, and Li_5TiN_3). The effective suppression of NH_3 obtained from the pellet with 30 wt. % MWCNTs-doped LiH was due to sufficient content and mechanical stability of LiH layers. Moreover, F substitution for H in LiH and Li_2NH to form $LiH_{1-x}F_x$ and $Li_2NH_{1-y}F_y$, respectively, were observed during dehydrogenation of the pellet with 30 wt. % MWCNTs-doped LiH. These phases likely benefited de/rehydrogenation kinetics and reversibility of the Li-N-H system.

CURRICULUM VITAE

Name   Miss Chongsutthamani Sitthiwet

Date of Birth   9th August 1991

Place of Birth   Nakhonrachsima, Thailand

Education (Include dates, Major and Details of Degrees, University)

  2010-2013   B.Sc. (Chemistry), Rajamankala University of Technology Isan. Thailand

  2014-2022   Ph.D. (Chemistry), Suranaree University of Technology, Thailand

Publications

Sitthiwet, C., Plerdsranoy, P., Dansirima, P., Eiamlamai, P., Utke, O., Utke, R. (2020) Improved hydrogen sorption kinetics of compacted $LiNH_2$-LiH based small hydrogen storage tank by doping with TiF_4 and MWCNTs. Journal of Alloys and Compounds, 832, 155026.

Sitthiwet, C., Plerdsranoy, P., Utke, O., Nijpanich, S., Chanlek, N., Eiamlamai, P., Utke, R. (2022) Hydrogen sorption kinetics and suppression of NH_3 emission of LiH-sandwiched $LiNH_2$-LiH-TiF_4-MWCNTs pellets upon cycling. Journal of Alloys and Compounds. 909, 164673.

Grants and Fellowships   Thailand Graduate Institute of Science and Technology (TGIST)

The Thailand Research Fund (TRF)